JGR Oceans

Key Points:

- Tides dominate the semidiurnal variability of the Hanna Shoal region in winter during periods of high sea ice cover
- Semidiurnal internal tides exist in the eastern Hanna Shoal region, while the tides are largely barotropic in the west
- Semidiurnal internal tides induce current shear that, potentially, erodes lower-layer stratification in winter

Supporting Information:

Supporting Information may be found in the online version of this article.

Correspondence to:

Y.-C. Fang,
ying-chih.fang@mail.nsysu.edu.tw

Author Contributions:

Conceptualization: Ying-Chih Fang
Data curation: Ying-Chih Fang, Hank Statscewich
Formal analysis: Ying-Chih Fang
Funding acquisition: Ying-Chih Fang
Investigation: Ying-Chih Fang, Hank Statscewich
Methodology: Ying-Chih Fang
Project Administration: Ying-Chih Fang, Hank Statscewich
Resources: Ying-Chih Fang, Hank Statscewich
Software: Ying-Chih Fang, Hank Statscewich
Supervision: Ying-Chih Fang

Semidiurnal Internal Tides Observed on the Eastern Flank of Hanna Shoal in the Northeastern Chukchi Sea

Ying-Chih Fang[1,2] [ID], **Markus Janout[2]** [ID], **Yusuke Kawaguchi[3]** [ID], **and Hank Statscewich[4]** [ID]

[1]Department of Oceanography, College of Marine Sciences, National Sun Yat-sen University, Kaohsiung, Taiwan, [2]Alfred Wegener Institute Helmholtz Center for Polar and Marine Research, Bremerhaven, Germany, [3]Atmosphere and Ocean Research Institute, The University of Tokyo, Kashiwa, Japan, [4]College of Fisheries and Ocean Sciences, University of Alaska Fairbanks, Fairbanks, AK, USA

Abstract This paper investigates the role of semidiurnal tides in the Hanna Shoal region on the northeastern Chukchi Sea shelf to evaluate their impact on the regional shelf dynamics. The study is based on 2-year long velocity time series from five oceanographic moorings. These records indicate the dominance of wind-generated near-inertial energy during the summer season with low ice cover. However, when the ocean is fully covered by sea ice, tides dominate the variability in the semidiurnal energy band. The records reveal considerable seasonal variability as well as regional differences, where barotropic tides dominate in the well-mixed waters west of Hanna Shoal while bottom-trapped internal (depth-dependent) tides are observed east of Hanna Shoal, where stratification can persist year-round. Resulting tide-driven shear in winter east of Hanna Shoal under stratified conditions can occasionally reach the level of a Richardson number below 1 and can be as low as ~0.25, implying the likelihood of shear instability and potentially eroding lower water column stability. This may lead to upward fluxes of near-bottom nutrient-rich Winter Water and thus carries ecosystem implications. Our study indicates that the internal tides east of Hanna Shoal are modulated by the spring-neap cycle and result from the interaction of barotropic tides with local bathymetry and stratification.

Plain Language Summary We investigated currents, temperature, and salinity records from five oceanographic moorings around Hanna Shoal in the northeast Chukchi Sea in the Arctic Ocean. The data indicate different water column structures and therefore different vertical structures of the tides between the east and west sides of Hanna Shoal. The water column on the west side is mainly homogeneous during winter, while the east side can remain stratified year-round. The presence of stratification then leads to vertical differences in tidal currents, which are larger in the lower part of the water column. Overall, our results indicate that tides interact with stratification and bottom topography east of Hanna Shoal. The resultant vertical tidal velocity differences have a potential to promote water exchange in the water column, even underneath an ice-covered ocean in winter and spring. This mechanism may supply important nutrients to the sunlit upper ocean in the spring and summer, and is thus potentially important for the Chukchi Sea ecosystem.

1. Introduction

The Chukchi Sea is located in the Pacific sector of the Arctic Ocean and receives a transport of ~1.1 Sv from the Pacific Ocean through Bering Strait (e.g., Woodgate, 2018; Woodgate et al., 2012). These nutrient-rich Pacific-origin waters (PW) undergo various modification processes while crossing the Chukchi shelf (e.g., Weingartner et al., 1998) en route toward the Arctic Ocean. The PW inflow induces high biological production, thus supporting a rich benthic ecosystem in the Chukchi Sea (Blanchard et al., 2017; Grebmeier et al., 2006, 2015). The transport of PW across the shelf is guided by the bathymetry and dominated by three major flow pathways (Figure 1a, e.g., Spall, 2007; Weingartner et al., 2005): the Alaskan Coastal Current branch in the east (e.g., Itoh et al., 2013), the Central Channel branch crossing the central shelf (Weingartner et al., 2005), and the Herald Canyon branch in the west.

Hanna Shoal is located in the center of the northeastern Chukchi shelf current system (Figure 1). Hanna Shoal is a regional biological hotspot (Grebmeier et al., 2015), presumably sustained by the circulation of nutrient-rich, cold (<−1°C), and saline (>32.5) Winter Waters (WW) (e.g., Danielson et al., 2017; Pickart et al., 2016). WW is formed in winter during sea ice production, particularly during polynya events (Ladd et al., 2016), which result in brine rejection and convective mixing of the water column. WW is commonly

Validation: Ying-Chih Fang, Hank Statscewich

Visualization: Ying-Chih Fang, Hank Statscewich

Writing – original draft: Ying-Chih Fang, Markus Janout, Yusuke Kawaguchi, Hank Statscewich

Writing – review & editing: Ying-Chih Fang, Markus Janout, Yusuke Kawaguchi, Hank Statscewich

observed on the northeastern Chukchi shelf from March (Fang et al., 2020, hereafter referred to as F20) until June–July (Gong & Pickart, 2015; Pickart et al., 2016). In late summer, WW on the southern shelf is gradually replaced by the northward progressing warmer (∼2°C–5°C) and less saline (∼31) Bering Sea Summer Water (BSSW). Replacement of WW does not seem to occur in the Hanna Shoal region, where WW remains present within ∼20 m of the bottom as observed during September surveys (e.g., Lin et al., 2019; Weingartner, Fang, et al., 2017).

In general, the waters around Hanna Shoal become well-mixed in winter, but are stratified in summer due to the presence of near-bottom WW or mid-water BSSW underneath a cold and meltwater-influenced fresh surface layer. The vertical distribution of these water masses forms a two-layer water column in late summer around Hanna Shoal, separated by a strong pycnocline (Fang et al., 2017; Weingartner, Fang, et al., 2017). However, recent work indicates that the water column east of Hanna Shoal remains stratified year-round (Weingartner, Fang, et al., 2017; F20). This stratification is maintained by sea ice melt and by lateral advection of Beaufort shelf waters from Barrow Canyon (Weingartner, Danielson, et al., 2017), and from the shelfbreak jet and the Chukchi Slope Current (Corlett & Pickart, 2017; Li et al., 2019; Llinás et al., 2009) (Figure 1b). The low-frequency flow field in response to this stratification east of Hanna Shoal is vertically sheared with an upper-layer northwestward baroclinic flow (F20; see red arrow in Figure 1b). As will be shown later, band-frequency currents, such as tides, also behave differently compared to regions west of Hanna Shoal.

Tides in the Chukchi Sea are generally weak (1–3 cm s^{-1}) (Baumann et al., 2020; Plueddemann et al., 1998), in comparison to the moderate tides (5–12 cm s^{-1}) of the Laptev Sea (Janout & Lenn, 2014) and much stronger tides (70–100 cm s^{-1}) in the Barents Sea (Poulain & Centurioni, 2015). Ambiguity in the semidiurnal currents (with a flow cycle about twice a day) between inertial motions and the M_2 tide occurs near the critical latitude (74.48°N, Figure 1a), where the M_2 frequency equals the local inertial frequency, f, and results in enhanced clockwise (CW) polarized tidal currents (Furevik & Foldvik, 1996). Note that the CW-polarized velocity field in time is also a signature of wind-generated (or generated by hybrid wind-sea ice movement) near-inertial internal wave (NIW) (e.g., Alford et al., 2016; D'Asaro et al., 1995; Kawaguchi et al., 2019). Separating NIW from the M_2 tide near the critical latitude was discussed by Pnyushkov and Polyakov (2012) on the continental slope (∼78.43°N) of the Laptev Sea. A great care should be taken if there exists a background relative vorticity field ζ, then frequencies of freely propagating internal waves fall within the range of buoyancy frequency (N) and $f + 0.5ζ$ (Kunze, 1985). Thus, it may be possible the M_2 tide and NIW co-exist within the same frequency band if ζ is included. Pnyushkov and Polyakov (2012) only yielded marginal frequency resolution (∼0.00002 cph) to differentiate these two signals, and therefore the component resulted from NIW in the semidiurnal currents may be retained in the predicted semidiurnal tidal currents. The tidal phase is expected to be fairly consistent through the year and can be quantitatively retrieved by long-term time series. In contrast, the more variable phase of intermittent NIW signals can be identified as the residual after stable tides are removed from the time series. A common practice is to isolate the NIW signal from a de-tided data set by removing barotropic tides estimated either from depth-averaged currents or from a tidal model (e.g., Arctic Ocean Tidal Inverse Model, 5 km, as known as AOTIM-5. See, Padman & Erofeeva, 2004; Padman et al., 2020). Rainville and Woodgate (2009) applied the former approach and found considerable seasonal variability in the NIW field on the north-central Chukchi Sea shelf from a 2-year long mooring record (see gray squares in Figure 1a for location). They found a distinct seasonality associated with sea ice presence that effectively dampens NIW-induced mixing, and results in a relatively quiescent environment during ice-covered periods. This portion of the shelf (and west of Hanna Shoal) becomes well-mixed by subsequent cooling and convection in winter. In the eastern Hanna Shoal region, however, stratification can persist through the winter (F20), based on two vertically-separated Conductivity-Temperature-Depth (CTD) sensors moored at the two individual moorings at the 50- and 60-m isobaths, respectively. The interaction between the semidiurnal tides with the flow field and stratification has not yet been investigated in the region and will be the focus of this paper based on 2012–2014 mooring records.

The paper is structured as follows. We provide an overview of the data and analyzing methods in Section 2. In Section 3 we present the observations and underline the spatial and seasonal variability of semidiurnal currents around Hanna Shoal, followed by a discussion and conclusion in Sections 4 and 5.
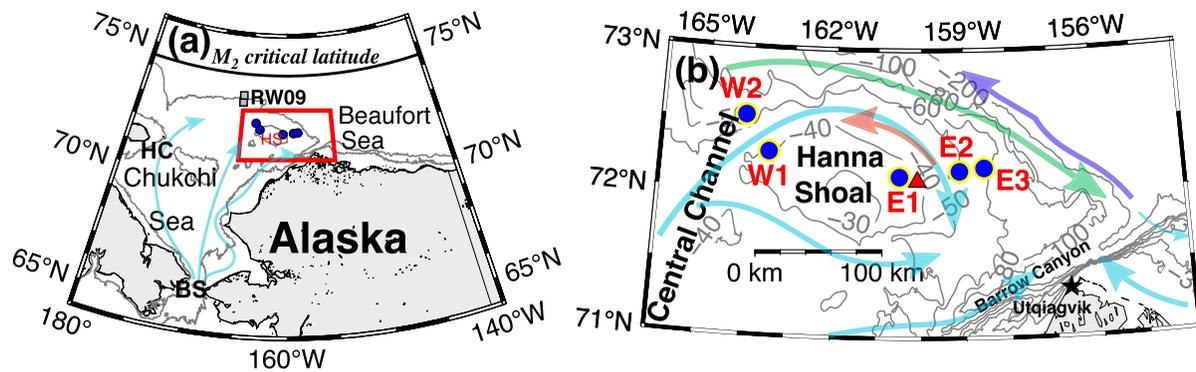
Figure 1. (a) Regional map showing the study area (red box) in the Chukchi Sea. Blue arrows denote the three major flow pathways. HC indicates Herald Canyon, BS is for Bering Strait, and HS denotes Hanna Shoal. The 40- and 200-m isobaths are shown. The gray squares denoting RW09 indicate the moorings used by Rainville and Woodgate (2009). The black curve is the M_2 critical latitude (see text) near 74.5°N. (b) Mooring locations (blue dots) in the study area. The red triangle denotes the North American Regional Reanalysis wind grid point representative of the regional winds. The black star denotes the village of Utqiagvik. Bathymetric contours are at 10-m intervals for 10–100 m. Blue arrows represent the background circulations around Hanna Shoal, the red arrow is for the upper-layer baroclinic flow east of Hanna Shoal, and green and purple arrows for the shelfbreak jet and Chukchi Slope Current, respectively.

2. Data and Methods

2.1. Mooring and Shipboard Data

Velocity measurements with 30-min intervals and 1-m vertical bins were obtained from five bottom-mounted, upward-looking Acoustic Doppler Current Profiler (ADCP) moorings (Weingartner et al., 2022) as part of the Chukchi Sea Offshore Monitoring in Drilling Area (COMIDA, Dunton et al., 2017) program. The moorings were deployed on the western (W1 and W2) and eastern (E1, E2, and E3) flanks of Hanna Shoal (Figure 1b), recording data from August 2012 to September 2014, with one turnover in September 2013. Moorings W1, E1, E2, and E3 were equipped with RDI 300 kHz ADCPs while an RDI 600 kHz ADCP was used at W2. These two data sets are investigated individually and are referred to by their year of deployment, for example, E1 2012-13 indicates the August 2012–September 2013 record for mooring E1. The ADCPs were configured with ∼180–200 pings per ensemble as a balance between battery consumption and data quality. The estimated standard errors in a ∼2-hr period were ∼0.5 cm s^{-1}, which is much less than the ∼10–15 cm s^{-1} semidiurnal internal tides of interest. Moorings were located on the 40 m (W1 and E1), 50 m (W2 and E2), and 60 m (E3) isobaths. For further mooring details please refer to Dunton et al. (2016) and F20. The mooring-based tidal characteristics vary little between neighboring sites but considerably between east and west. Therefore, to underline regional differences around Hanna Shoal we will specifically focus on W2 and E2.

CTD measurements collected with two Seabird SBE 37 MicroCATs at mid-depth and near-bottom at both E2 and E3 for the 2012-13 period are used to derive stratification east of Hanna Shoal. Note that these are the only available wintertime stratification observations around Hanna Shoal. Other moorings were only equipped with one near-bottom MicroCAT (F20). To compare concurrent near-bottom conditions west of Hanna Shoal, we also incorporated measurements from W2 2012-13. Temperature and salinity accuracies were ∼0.002°C and ∼0.002, respectively, sampled with 15-min intervals.

CTD data at each of the mooring sites, collected during the two COMIDA cruises (Weingartner, Fang, et al., 2017) in 2012 and 2013, were used to derive profiles of buoyancy frequency (N) and to compute the baroclinic mode F_m by solving the Sturm-Liouville problem (e.g., Kundu et al., 2012; Wang et al., 2013):

$$\frac{\partial}{\partial z}\left(\frac{f^2}{N^2}\frac{\partial F_m}{\partial z}\right) = -\frac{1}{R_m^2}F_m \tag{1}$$

$$\frac{\mathrm{d}F_m}{\mathrm{d}z} = 0 \text{ at } z = 0, -H \tag{2}$$

where R_m is the Rossby deformation radius for the mth baroclinic mode and H is the bottom depth. In this paper the first baroclinic mode ($m = 1$) internal wave structure is predominant in our data so only F_1 will be shown. We acknowledge that the above modal calculations are based on the flat bottom assumption. If considering rough

bathymetry, then the bottom boundary condition requires no horizontal flow at the bottom ($F_m = 0$), as suggested by historic current meter observations (e.g., Wunsch, 1997). The calculated baroclinic modes will be modified accordingly and result in a larger deformation radius (de La Lama et al., 2016; LaCasce & Groeskamp, 2020). We found that R_1 will increase from ∼2.6 to ∼3.5 km based on the rough bathymetry boundary condition, consistent with the findings by LaCasce and Groeskamp (2020). However, the zero near-bottom flow does not apply here, as persistent near-bottom currents forced by the large-scale Pacific-Arctic pressure gradient are known to occur on the Chukchi shelf (e.g., F20).

2.2. Harmonic Analysis

Conventional spectral analyses using record-length velocity data have shown that the semidiurnal energy is about 1–2 orders of magnitude greater than the diurnal energy (F20). However, only about 10%–30% variance is explained by the tides based on depth-averaged currents using the T_TIDE harmonic analysis toolbox (Pawlowicz et al., 2002), developed from the Fortran software by Foreman (1977). The weak tides, combined with the difficult differentiation between semidiurnal tides and inertial currents, and a vertically-sheared flow east of Hanna Shoal makes the use of record-length and depth-averaged time series for harmonic tidal analysis questionable. We therefore truncated our time series into monthly records and computed the monthly tidal currents $t_m(z)$ at all available depths z, using T_TIDE. The results of $t_m(z)$ were compared in terms of complex correlation magnitudes following Kundu (1976, cf., their Equation 3.4) with the model-derived semidiurnal tidal currents (including four major semidiurnal tidal constituents: M_2, S_2, N_2, and K_2), t_{AOTIM}, from the AOTIM-5 barotropic tidal model (Padman et al., 2020). A monthly correlation $Cor(z)$ between $t_m(z)$ and t_{AOTIM} was then computed for all depths. The depth-averaged correlation, $\overline{\sum Cor(z)}$ (the overbar denotes depth-averaging), for all z depths is used to better characterize the seasonality and characteristics of the semidiurnal tides once the wind-generated inertial currents are reduced with a growing sea ice cover. We also examined two other tidal models archived in the Arctic Data Center, the 5-km resolution Arc5km2018 (Erofeeva & Egbert, 2020), and the 2-km resolution Arc2kmTM (Howard & Padman, 2021). These two models yielded similar results and did not affect our scientific conclusions, so model-derived semidiurnal tides will be based on t_{AOTIM} in this paper.

2.3. Winds, Sea Ice Concentrations, and ADCP-Derived Sea Ice Drift Velocities

We used the 3-hourly, unfiltered, 10-m surface two-dimensional horizontal winds, $\overrightarrow{U}_{wind}$, from the North American Regional Reanalysis (NARR) (Mesinger et al., 2006) and chose the grid point (red triangle in Figure 1b) closest to the E1 mooring to be representative of the local winds. We computed the wind work by

$$\text{Windwork} = \rho_{air} C_d |\overrightarrow{U}_{wind}|^3. \tag{3}$$

where ρ_{air} is the air density (1.225 kg m^{-3}) and C_d is the drag coefficient of 1.25×10^{-3} following Kara et al. (2007).

Sea ice concentration (SIC, %) was obtained from satellite products as well as from the moored ADCPs. Remotely-sensed SIC was generated by Nimbus-7 SMMR and DMSP SSM/I-SSMIS Passive Microwave Data and were retrieved from the grid points closest to each mooring from the National Snow and Ice Data Center (NSIDC, https://nsidc.org/data/nsidc-0051#). These data have spatial and temporal resolutions of 25 km and 1 day. We used the NSIDC-derived SIC to describe the long-term sea ice evolution.

The "bottom-tracking" function of the ADCPs allowed the derivation of two-dimensional ice drift velocities ($\overrightarrow{U}_{ice}$) and SIC (here we define it as SIC_{ADCP}) at the mooring site, following the methodology of Visbeck and Fischer (1994) with additional details discussed by Stoudt (2015). We examined the variability of total surface stress τ_{Total} including contributions from wind speed and sea ice drift by

$$\overrightarrow{\tau}_{Total} = SIC_{ADCP} * \overrightarrow{\tau}_{ice-water} + (1 - SIC_{ADCP}) * \overrightarrow{\tau}_{air-water}. \tag{4}$$

where $\overrightarrow{\tau}_{ice-water}$ and $\overrightarrow{\tau}_{air-water}$ are ice-water and air-water interfacial stresses following Yang (2006) and are described by the following equations

$$\overrightarrow{\tau}_{ice-water} = \rho_{water} C_{iw} |\overrightarrow{U}_{ice} - \overrightarrow{U}_{ocean}| \left(\overrightarrow{U}_{ice} - \overrightarrow{U}_{ocean} \right). \tag{5}$$

$$\vec{\tau}_{\text{air}-\text{water}} = \rho_{\text{air}} C_{\text{d}} |\vec{U}_{\text{wind}}| \vec{U}_{\text{wind}}. \tag{6}$$

where ρ_{water} is the water density (1,024 kg m^{-3}) and $C_{\text{iw}} = 0.0055$ is the ice-water drag coefficient (Hibler, 1979). $\vec{U}_{\text{ocean}}$ is the upper-layer ocean velocity and is determined by the ADCP-derived 40-hr low-passed currents (from F20) at the uppermost bin. Magnitudes of these stresses ($\tau_{\text{Total}} = |\vec{\tau}_{\text{Total}}|$, $\tau_{\text{ice}-\text{water}} = |\vec{\tau}_{\text{ice}-\text{water}}|$, and $\tau_{\text{air}-\text{water}} = |\vec{\tau}_{\text{air}-\text{water}}|$) are used for later analyses. The calculation of τ_{Total} is to ascertain that observed features in winter are not associated with the surface forcing.

We also computed the wind factor, which is defined as

$$\text{Wind factor} = |\vec{U}_{\text{ice}}|/|\vec{U}_{\text{wind}}|. \tag{7}$$

The wind factor reflects the ice response to wind forcing, where a larger wind factor resembles faster sea ice drift. We find typical wind factors in our data peaked at about 0.1 and ranging from ~0.03–0.06 as SIC >50%, comparable with Martini et al. (2014) who provided wind factors ranging from ~0.01–0.1 in the neighboring Beaufort Sea.

2.4. Data Processing for Semidiurnal Currents

To better investigate the role of tides in winter, we separated the records into a low sea ice cover period (LSP, 1 July–30 November) and a high sea ice cover period (HSP, 1 December–30 June). Unfiltered velocities were first band-passed with a fourth-order 8–16-hr cutoff Butterworth filter and then grouped into LSP and HSP periods accordingly. Baumann et al. (2020) examined available current profile time series throughout the Arctic to construct an Arctic tidal current atlas. They concluded that a clear separation of wind-driven inertial energy from semidiurnal tidal currents is not possible around the critical latitude and that their combined effects have to be evaluated jointly. As will be shown in Section 3, separation of the data into LSP and HSP can better isolate the semidiurnal tidal signals. Band-passed complex velocities at each depth during the two defined periods were used to compare semidiurnal rotary spectra (e.g., Emery & Thomson, 1997; Gonella, 1972). Since all semidiurnal tidal components rotate CW from the harmonic analysis and our computed CW spectra are about two orders of magnitudes greater than the counterclockwise (CCW) components in both LSP and HSP, only CW spectra will be shown.

We used the complex empirical orthogonal function (CEOF) technique by Edwards and Seim (2008), and will show in Section 3.3 that this method more effectively captures the tidal bottom boundary layer (BBL). The CEOF method is identical to the traditional EOF analysis but utilizes the complex time series (e.g., $u + iv$, where u and v are respectively zonal and meridional components of the flow and $i = \sqrt{-1}$). The CEOF eigenfunctions detect statistically-coherent signals in terms of modal structures derived from the data. The first two CEOF eigenmodes explain ~80% of the total variance. Individually, the explained variance of Mode-1 is ~2–8 times greater than that of Mode-2, thus only Mode-1 eigenfunctions will be shown.

2.5. Analytical Tidal BBL Model

Following Danielson and Kowalik (2005, details are described in their appendix), the linear and barotropic equations of motions are solved, and the frictional velocities within the BBL may be modeled as follows:

$$\frac{\partial q_1}{\partial t} - i f q_1 = A_z \frac{\partial^2 q_1}{\partial z^2}. \tag{8}$$

$$\frac{\partial r_1}{\partial t} + i f r_1 = A_z \frac{\partial^2 r_1}{\partial z^2}. \tag{9}$$

where q_1 and r_1 indicate CW and CCW frictional velocities, respectively, and z is the vertical coordinate starting from the bottom, and A_z is a parameterized eddy viscosity for vertical exchange of momentum. After applying
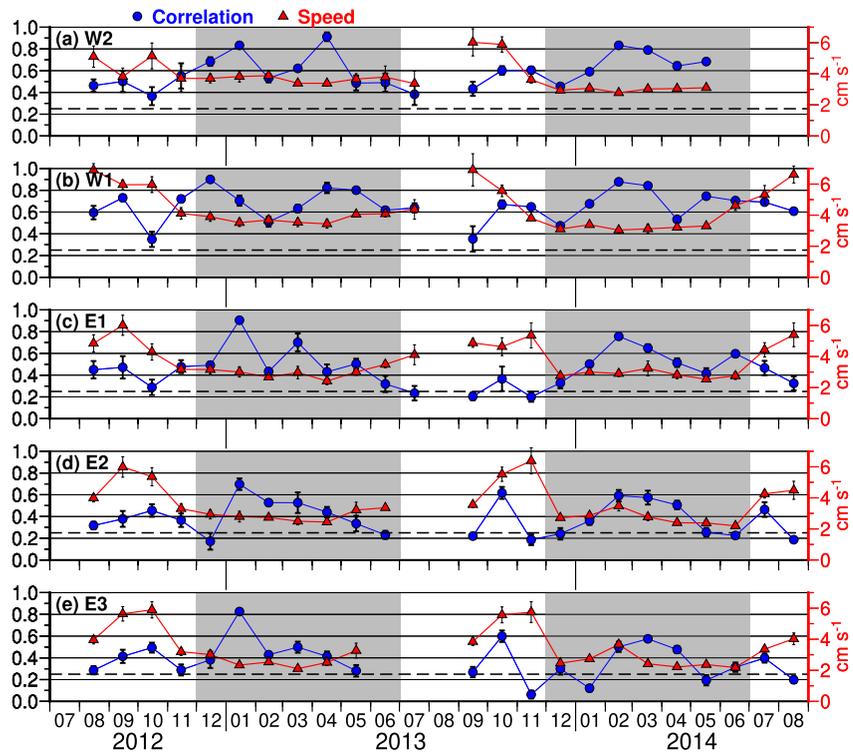
Figure 2. Depth-averaged correlation (blue dots), for each monthly, derived from an average between observed tidal currents $t_m(z)$ and the monthly values provided by the AOTIM-5 barotropic tidal model t_{AOTIM} at all available z depths for (a) W2, (b) W1, (c) E1, (d) E2, and (e) E3. Note that 2012-13 W2 data are only available below 25 m. Red triangles are the monthly depth-averaged 8–16 hr band-passed current speed. Vertical error bars are the 95% confidence interval estimated by using the student's t distribution. Gray shading denotes the high sea ice cover periods. The 95% significance level (horizontal dashed line) is estimated from the effective number of degrees of freedom with the integral time scale of 12 hr.

boundary conditions and assuming constant A_z, we may compute the CW component of the flow (sum of background geostrophic flow and frictional velocities):

$$q(\omega_{M_2}, z, f, t) = q_0 \left\{ 1 - \frac{\cosh\left[\lambda_1(z - H)\right]}{\cosh(\lambda_1 H)} \right\} \exp\left(-i\omega_{M_2}t\right). \tag{10}$$

Here, ω_{M_2} is the M_2 frequency and q_0 denotes the background geostrophic flow. For locations south of the critical latitude of the M_2 tide in the northern hemisphere:

$$\lambda_1 = (1 - i)\sqrt{\frac{(\omega_{M_2} - f)}{2A_z}}. \tag{11}$$

Thus, we can use Equation 10 with estimated values of A_z and q_0 and $H = (40, 50, 60)$ m to gain insight into the structure of the BBL at the mooring sites. Our data do not allow a quantitative estimate of A_z, so for simplicity we adopt a constant $A_z = 0.5 \times 10^{-4} \text{ m}^2 \text{ s}^{-1}$ guided by the model configuration using $10^{-4} \text{ m}^2 \text{ s}^{-1}$ for studying the circulation on the Chukchi Sea shelf (Spall, 2007; Watanabe et al., 2017, 2022). We use $q_0 = 5 \text{ cm s}^{-1}$, which is a typical value of the mean flow (e.g., F20).

3. Results

3.1. Spatial Variability of Semidiurnal Currents

Monthly segments of observation-based tidal currents $t_m(z)$ at each z depth derived from harmonic analysis (Section 2.2) are compared with model-based semidiurnal tidal currents t_{AOTIM} for all data sets in a correlation analysis, which yields a depth-averaged correlation each month (Figure 2). The records indicate a slight

Table 1
Averaged Correlations During Low and High Sea Ice Cover Periods

	2012–13 LSP		2013–14 LSP		2012–13 HSP		2013–14 HSP	
	Mean	95% CI	Mean	95% CI	Mean	95% CI	Mean	95% CI
W2	0.45	0.10	0.55	0.25	0.65	0.16	0.67	0.14
W1	0.61	0.19	0.59	0.17	0.71	0.13	0.69	0.14
E1	0.38	0.14	0.31	0.14	0.54	0.18	0.54	0.13
E2	0.38	0.09	0.33	0.24	0.42	0.17	0.39	0.15
E3	0.37	0.16	0.31	0.25	0.47	0.20	0.35	0.25

Note. The 95% confidence intervals (95% CI) estimated by the student's t distribution are also provided. LSP, low sea ice cover period; HSP, high sea ice cover period.

seasonality, with generally higher correlations during the HSP (see gray shading in Figure 2; Table 1), suggesting that the observed tidal currents in winter were dominated by the semidiurnal tides. Monthly correlations west of Hanna Shoal were overall higher and uncertainties ($\sim\pm0.03$, estimated using the student's t distribution) were generally smaller than those in the east ($\sim\pm0.05$), in particular at station W1 where correlations were mostly >0.6 (Figure 2; Table 1). This may suggest that $t_m(z)$ can be well represented by the barotropic t_{AOTIM} and that vertical shear of $t_m(z)$ was small, implying rather barotropic semidiurnal tidal currents west of Hanna Shoal. On the eastern side of Hanna Shoal (E1, E2, and E3), the correlation was <0.6 over most of HSP (Table 1) with a larger uncertainty, and for some months the correlation was not significant at all (e.g., Figures 2d and 2e). We also computed monthly, depth-averaged, band-passed current speeds for each mooring (see red triangles, Figure 2). There is a clear trend that the band-passed currents weakened $\sim50\%$ from ~6 cm s^{-1} in LSP to about 2–3 cm s^{-1} in HSP. This reflects the wind-driven inertial energy being impeded by the sea ice so the band-passed currents during HSP are dominated by the semidiurnal tides. This pattern may be analogous to the results of low inertial current magnitudes made by Rainville and Woodgate (2009, cf., their Figure 2) when sea ice cover is present in the Chukchi Sea.

The thermohaline properties at E2 2012-13 and E3 2012-13 showed considerable variability throughout the records (Figure 3). The temperature ranged between −1.6°C and 1°C during September–December 2012, with decreasing mid-depth (25 and 32 m) temperatures to the freezing point after January 2013 until the following summer (see red lines in Figures 3a and 3c). Mid-depth salinities underwent a sharp decrease from ~32.5 to ~29 in late December 2012 (see red lines in Figures 3b and 3d). This freshening likely resulted from the erosion of the summer pycnocline, initiated by surface cooling and subsequent convective mixing and mixed layer deepening. This is a common evolution in winter that was previously observed in several Chukchi shelf regions
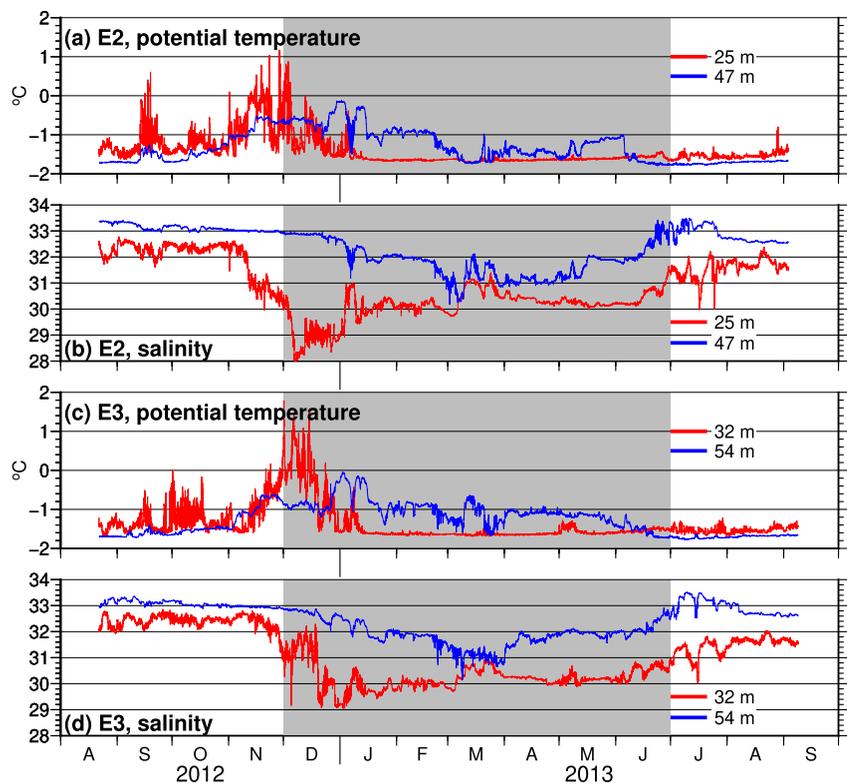

Figure 3. Time series of (a) potential temperature and, (b) salinity at mid-depth (red) and near-bottom (blue) for mooring E2, and (c, d) for E3. Gray shading denotes the high sea ice cover period.
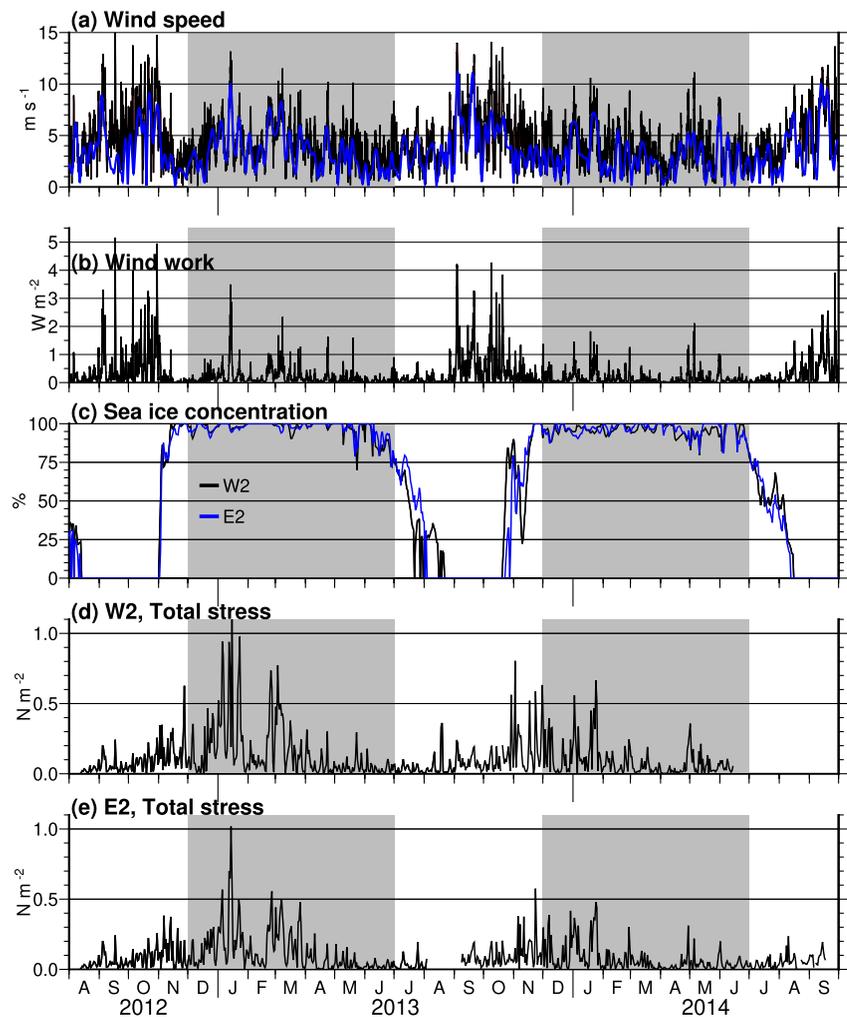
Figure 4. Time series of (a) daily wind speed (m s^{-1}, black) and 7-day low-passed wind speed with a 9th-order 40-hr Butterworth filter (blue), (b) daily wind work from Equation 3 (in W m^{-2}), (c) sea ice concentration (in %) from National Snow and Ice Data Center at W2 (black) and E2 (blue), and τ_{Total} (in N m^{-2}, from Equation 4) at (d) W2 and (e) E2. Gray shading denotes the high sea ice cover periods.

(Ladd et al., 2016; Stabeno et al., 2018; Weingartner et al., 2005). However, apparent regional contrasts include the above-freezing near-bottom temperatures east of Hanna Shoal during January–June 2013 (see blue lines in Figures 3a and 3c), which were likely sustained by the salinity-controlled stratification. At the western Hanna Shoal, the near-bottom temperatures evolved equally as the mid-depth temperatures at E2 (see F20, their Figure 10). The only exception characterizing near-bottom temperature drops were found at E2 around 10–19 March 2013 (see blue line Figure 3a). This was related to the spreading of newly-formed saline WW from coastal polynyas (Stabeno et al., 2018; F20), although it was not the case at E3.

NIW generation is dominated by spatial-temporal fluctuations of the local wind stress in the ice-free oceans (e.g., D'Asaro, 1985a; Pollard & Millard, 1970) or sea ice motion in response to passing storms (e.g., Fer, 2014; Martini et al., 2014). The wind speed varies seasonally with generally stronger winds of up to ~15 m s^{-1} before the HSP (Figure 4a). Strong winds were not as frequent during the fall months and increased to 10–13 m s^{-1} once sea ice developed during winter. On weekly timescales (7-day low-passed wind speed, Figure 4a), such seasonality becomes less obvious. Wind work, on the other hand, reveals a clearer seasonality with a significantly smaller energy flux (<0.5 W m^{-2}) during the HSP, compared to the larger wind work (1–3 W m^{-2}) in summer and fall (Figure 4b). Intermittent increases in wind work may develop during HSP, but they were rarely above ~2 W m^{-2}. SIC was >90% for most of the HSP on both sides of Hanna Shoal, with occasional polynya events when SIC dropped to ~80% or less (Figure 4c, e.g., May 2013, April–May 2014). Combining winds and sea ice drift into
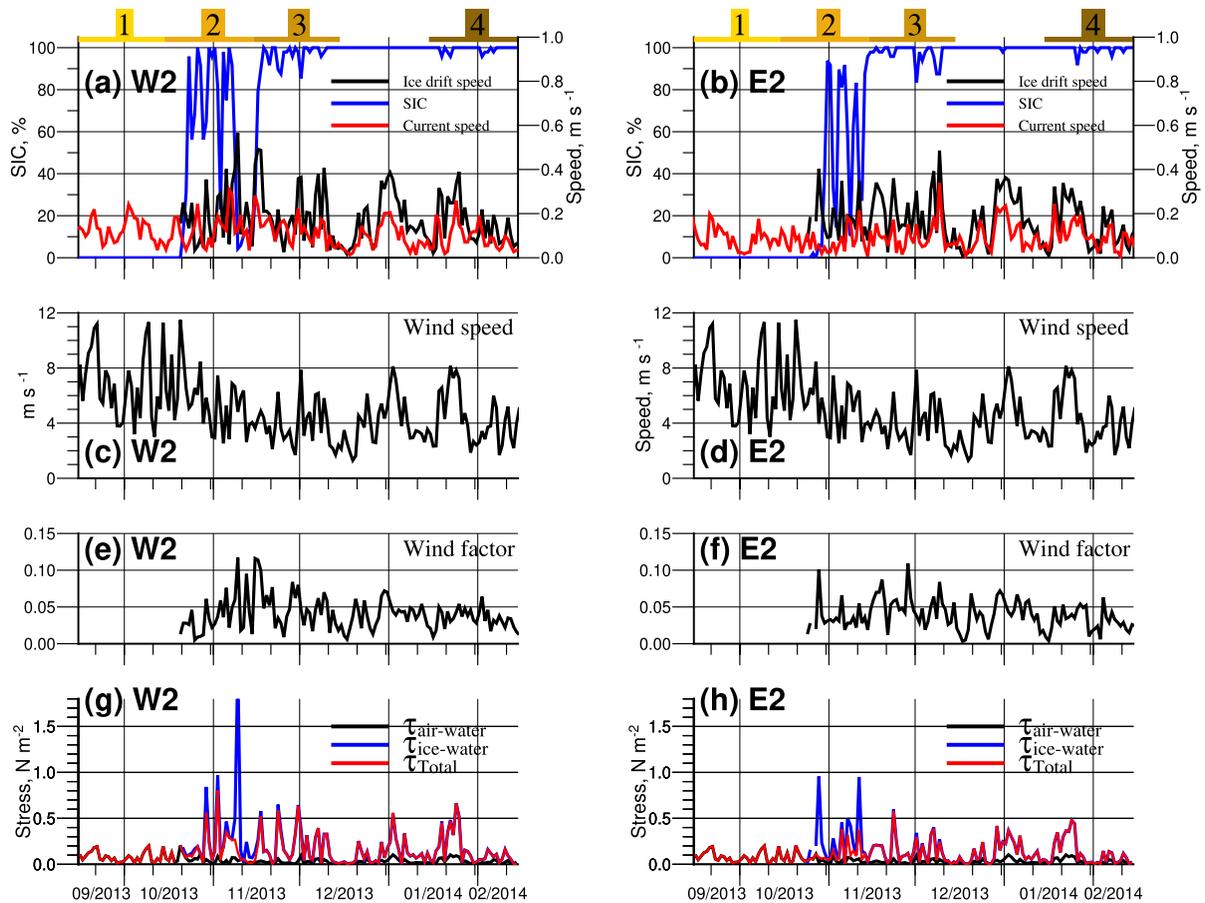
Figure 5. Daily Acoustic Doppler Current Profiler-derived sea ice concentration (blue), ice drift speed (black), and upper-layer ocean current speed (red, from F20) during 15 September 2013–15 February 2014 at (a) W2 (left panel) and (b) E2 (right panel). (c, d) Daily wind speed, (e, f) Wind factor (from Equation 7), and (g, h) τ_{Total} (red, from Equation 4), $\tau_{\text{ice-water}}$ (blue, from Equation 5), and $\tau_{\text{air-water}}$ (black, from Equation 6). Yellow labels showing 1–4 on top of (a) and (b) denote the time periods shown in Figure 6.

total stress reveals a seasonality where larger total stresses (∼0.5 N m^{-2}) occurred in the early months of HSP (Figures 4d and 4e). This may be related to more mobile sea ice in the early stage of an HSP, consistent with Schulze and Pickart (2012), who showed that enhanced upwelling on the Alaska Beaufort Sea shelf generally occurs in the partially ice-covered season due to overall increased surface stress.

An example shown in Figure 5 provides the relative contribution from wind, sea ice, and upper-layer ocean current (see panels a–d) to the total stress (see panels g–h) during the ice-growing period (see yellow labels 2 and 3 on top of the figure) on both sides of Hanna Shoal. It shows intermittent peaks in the total stress during the freeze-up period in November–December 2013 and emphasizes that drifting sea ice significantly contributes to the surface forcing. The wind factor (see panels e–f), as a measure for the ice in response to wind forcing, was ∼0.1 during the freeze-up period and decreased to ∼0.05 when the sea ice cover fully developed (i.e., SIC >95%). When the SIC developed, sea ice motion decreases and was more coherent with the underlying ocean currents and the surface winds (e.g., after January 2014). This is in line with the conditions on the Beaufort Sea shelfbreak in winter (Martini et al., 2014), showing that sea ice motion on Hanna Shoal is not inhibited. Sea ice and upper-layer ocean current appear to be resonant to the wind, but the observed semidiurnal-band currents were reduced by ∼50% (e.g., Figure 2). This suggests the fully-developed sea ice cover efficiently dampens the wind-driven inertial energy (e.g., McPhee, 1978). Examining wind- and ice-induced stresses on either side of Hanna Shoal (i.e., W2 and E2) highlights a seasonally-variable but region-wide coherent surface forcing.

The correlations between $t_m(z)$ and t_{AOTIM} from the five mooring sites (Figure 2) were highest during January–February and decreased thereafter, in particular east of Hanna Shoal. Before sea ice develops, substantial winds and associated wind work impact the upper ocean and generate near-inertial currents. This may explain the lower

correlation between $t_m(z)$ and t_{AOTIM} before HSP (Figure 2) and the lowest correlation during the mobile ice season in November–December when maximum surface stresses intensify near-inertial currents. When the sea ice cover is fully developed (e.g., after January), the wind impact reduces accordingly and the barotropic semidiurnal tides are more easily revealed. This is underlined by the higher correlations between $t_m(z)$ and t_{AOTIM} and smaller error bars, in particular at W1 and W2. On the eastern flank of Hanna Shoal (E1, E2, and E3), correlations between $t_m(z)$ and t_{AOTIM} are more depth-dependent with larger error bars, implying a baroclinic tidal structure. The lower and decreasing correlations as the HSP season progresses likely resembles the response to the developing stratification (e.g., Figure 3), but not to the surface forcing as previously discussed (Figure 4). These results hint at the existence of semidiurnal internal tides east of Hanna Shoal, in comparison to the barotropic semidiurnal tides prevalent in the west.

3.2. Seasonal Variability of Semidiurnal Currents

Regional differences in the temporal evolution of semidiurnal baroclinic currents become apparent in our September 2013 to February 2014 records from W2 (Figure 6, left panels) and E2 (Figure 6, right panels), which (other than the 2012-13 data) provides sufficient coverage of the upper ocean's currents. When the shelf was still ice-free before mid-October (Figures 6a and 6b, and see yellow label 1 in Figures 5a and 5b for SIC record) or only partially ice-covered before December (Figures 6c and 6d, and see yellow label 2 in Figures 5a and 5b for SIC record), NIW signals were ubiquitous on both sides of Hanna Shoal, with strong oscillatory currents of ~10–15 cm s^{-1} in the water column. Their appearances are largely in response to wind bursts and/or ice movements (e.g., Figure 5, total stress ~0.2–0.6 N m^{-2}), rather than to the fortnightly spring-neap tidal cycle. For example, wave packets were detected during the weakest tidal period (e.g., 26–29 September, Figures 6a and 6b; 23–28 October, Figures 6c and 6d), implying that they were likely not triggered by the barotropic tide.

The NIW signals rapidly diminished after 25 November (Figure 6e) once SIC reached ~100% (Figure 5). At W2, semidiurnal currents no longer varied in response to winds or ice movements. For example, there were two episodes of strong winds that resulted in large ice drift velocities (~40 cm s^{-1}) during 6–11 December (Figures 5a and 5b, see yellow label 3), but currents remained unaffected and relatively weak (<5 cm s^{-1}) (Figure 6e). The two-layered flow structure with opposing currents above and below 20–25 m shifted to a rather barotropic flow, aligned with the tidal period. This is consistent with F20 (see their Figure 10), who showed near-bottom temperatures at W2 decreasing from 0.5°C to near-freezing (−1.8°C) during the same time period, implying that stratification in the water column was indeed eroded due to surface cooling and convective overturning. Currents became stronger (from <2 to 5 cm s^{-1}) during the fortnightly spring tide (e.g., 3–5 December; 30 January–2 February), indicating that the barotropic semidiurnal tide dominates the semidiurnal variability in winter.

On the eastern Shoal at E2, near-surface currents showed surface-forced NIWs due to wind and ice motion (Figure 5; e.g., 1–4 December, Figure 6f). This suggests that shallow stratification might have still been present in the upper water column, which was unfortunately not resolved by our 2013-14 observations. Furthermore, the patterns presented in Figures 6f and Figure 6h showed amplified near-bottom (~15 cm s^{-1}) currents (e.g., 5–8 December, Figure 6f; 23–30 January; 6–11 February, Figure 6h), which were apparently decoupled from upper ocean currents and unlikely to be forced at the surface (see Figure 5). In this example, the amplified near-bottom flow in Figure 6f occurred during the spring tide, while that shown in Figure 6h occurred during the neap tide, overall implying that these amplified near-bottom semidiurnal currents are unrelated to the local tidal phase. Instead, it is suggestive of internal tidal currents generated by the interaction of internal tides with bathymetry and/or stratification. The change of phase also suggests that the observed internal tides have propagated from other places with a varying phase in response to varying ocean conditions.

3.3. Vertical Structure of Semidiurnal Currents

A typical water column during a LSP on the northeastern Chukchi Sea shelf is comprised of two layers with a ~10–20 m thick BSSW or meltwater layer underlain by the WW layer (Fang et al., 2017, 2020; Weingartner, Fang, et al., 2017). Layers can be identified by the profile of buoyancy frequencies N^2 and the corresponding first baroclinic mode F_1 derived from summer CTD observations (Figure 7). Due to the presence of WW underneath sea ice meltwater in late August, stratification was strong, ranging from ~3–8 × 10^{-3} s^{-2} around the pycnocline located at ~10–15 m. This yields the zero crossings of F_1 at the deeper depths of ~15–20 m, with the exception
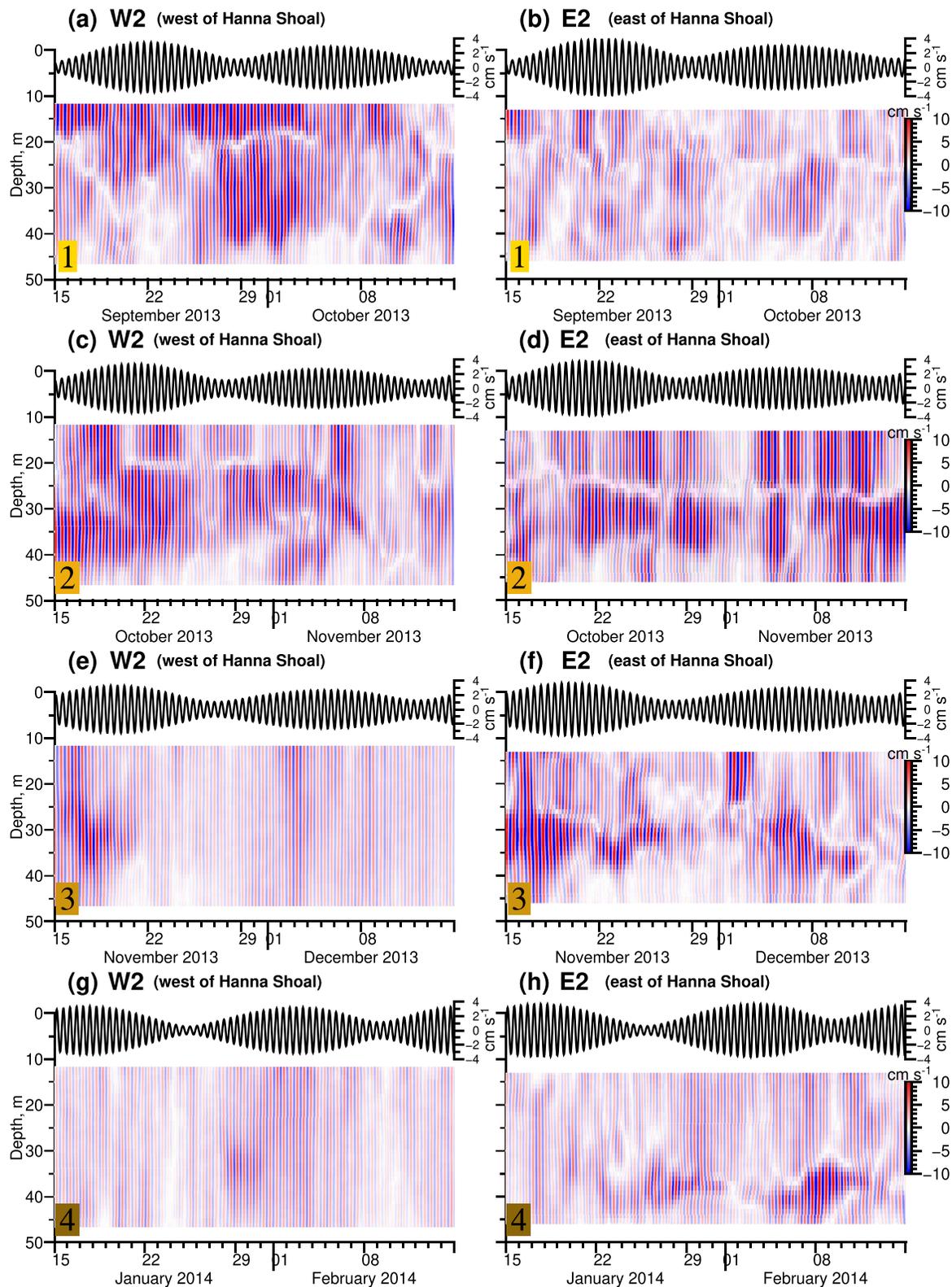
Figure 6. Band-passed zonal (u) current velocities (cm s^{-1}, colored shading) and the u-component of t_{AOTIM} (cm s^{-1}, black line at top of each panel) for western (W2, left panels) and eastern (E2, right panels) Hanna Shoal for (a, b) 15 September–15 October 2013 (marked as a yellow label with 1 in Figure 5) (c, d) 15 October–15 November 2013 (marked as a yellow label with 2 in Figure 5), (e, f) 15 November–15 December 2013 (marked as a yellow label with 3 in Figure 5), and (g, h) 15 January–15 February 2014 (marked as a yellow label with 4 in Figure 5).
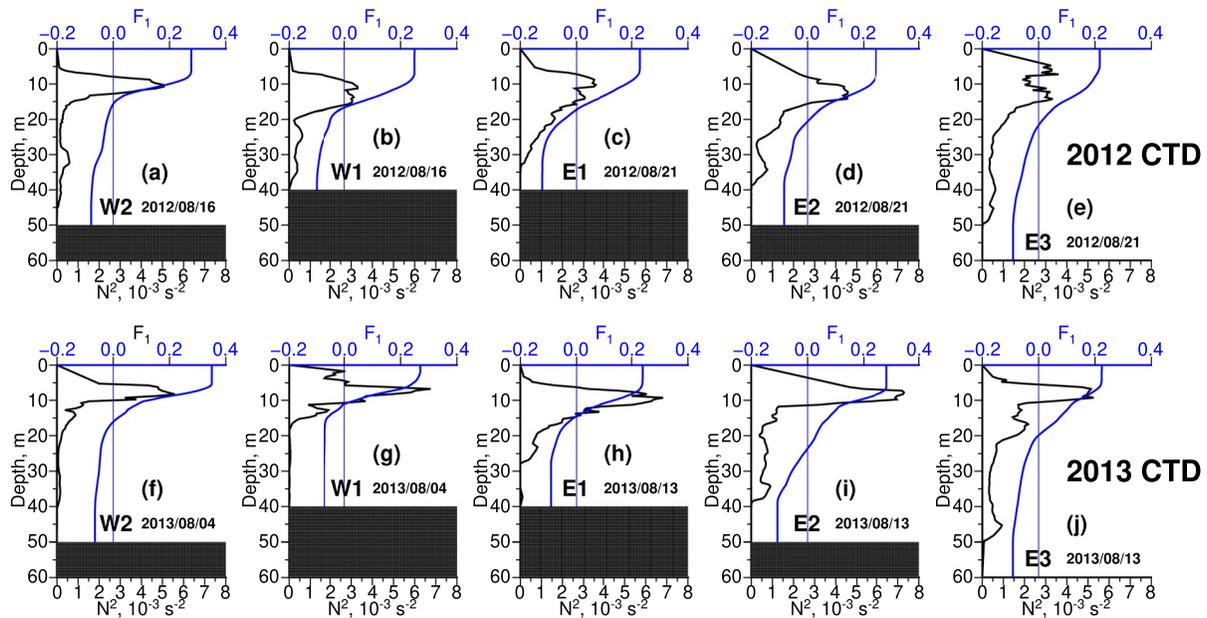
Figure 7. Buoyancy frequency (N^2 in s^{-2}, black) and the first baroclinic mode (F_1, unitless, blue) derived from summer Conductivity-Temperature-Depth (CTD) profiles at each mooring site in (a)–(e) 2012 and (f)–(j) 2013. Dates (yyyy/mm/dd) indicate the day of CTD measurements.

of E2 2013-14 where the zero-crossing of F_1 was at ~25 m. The location of the zero crossings can be used to guide the vertical structure of the observed currents, as this is the vertical structure of a simple linear internal wave based on the given stratification. These depth ranges agree well with the observed zero crossings of the horizontal currents in the vertical (Figures 6a–6d), and are consistent with other NIW observations on shallow shelves (MacKinnon & Gregg, 2005).

The CEOF eigenfunction is a complex quantity and can be viewed as a linear combination of both u and v components by which the maximum variance is captured (see Kaihatu et al., 1998). The amplitude structure for the CEOF Mode-1 has zero crossings near 20 m (Figure 8), similar to those of the baroclinic modes (Figure 7). Note that the near-zero bottom flow seen in the CEOF Mode-1 is in contrast to the flat bottom assumption used in the calculations of the baroclinic modes. More importantly, below this depth the phases in the lower water column yield a difference of ~180°, indicative of counter-flowing currents.

To gain further insights into the importance of the leading mode, we define α as the ratio between the explained variances (in %) of CEOF Mode-1 and Mode-2. Details of these values are provided by Table 2. During LSP, we found α ranging from 1.3–3.4 in 2012-13 and 1.6–2.1 in 2013-14, geographically coherent between the west and east sides of Hanna Shoal.

When the ocean is fully covered by sea ice in winter, the CEOF Mode-1 eigenfunctions (Figure 9) exhibit a structure that differs substantially from the two-layered structure dominating the LSP (Figure 8). The Mode-1 vertical profile resembles a classic tidal BBL with most shear within about 20 m above the bottom (see black arrows, Figure 9). Here the real and imaginary parts of eigenfunctions resemble the CW and CCW components in conventional harmonic analyses, respectively. The phase variations in the water column are much less than those during LSP, mostly within the range of ~10–20° differences above the bottom. This also reflects the nature of the rotating tidal BBL. Werner et al. (2003) investigated tidal BBL driven by semidiurnal tides under both weak and strong stratification on Georges Bank in the Atlantic Ocean. They found that the velocity profiles became more sheared in the lower water column with a local maximum at mid-depth when the ocean was stratified. The patterns of eigenfunctions and phases derived from the CEOF method shown in Figure 9 resemble the observed tidal BBL by Werner et al. (2003; compare with their Figures 5 and 13). One signature of the tidal BBL is the rotating velocity vector near the bottom. The CEOF-derived phases for the 2012-13 data showed veering of 10–20° in the lower part of the water column at all sites except W1 (red curves in Figures 9a–9e). The phase veering in 2013-14 was relatively small (<10°) at W1 and W2, in comparison to 10–20° for all eastern sites (red curves in Figures 9f–9j). The phase patterns during HSP do not indicate striking differences between east and
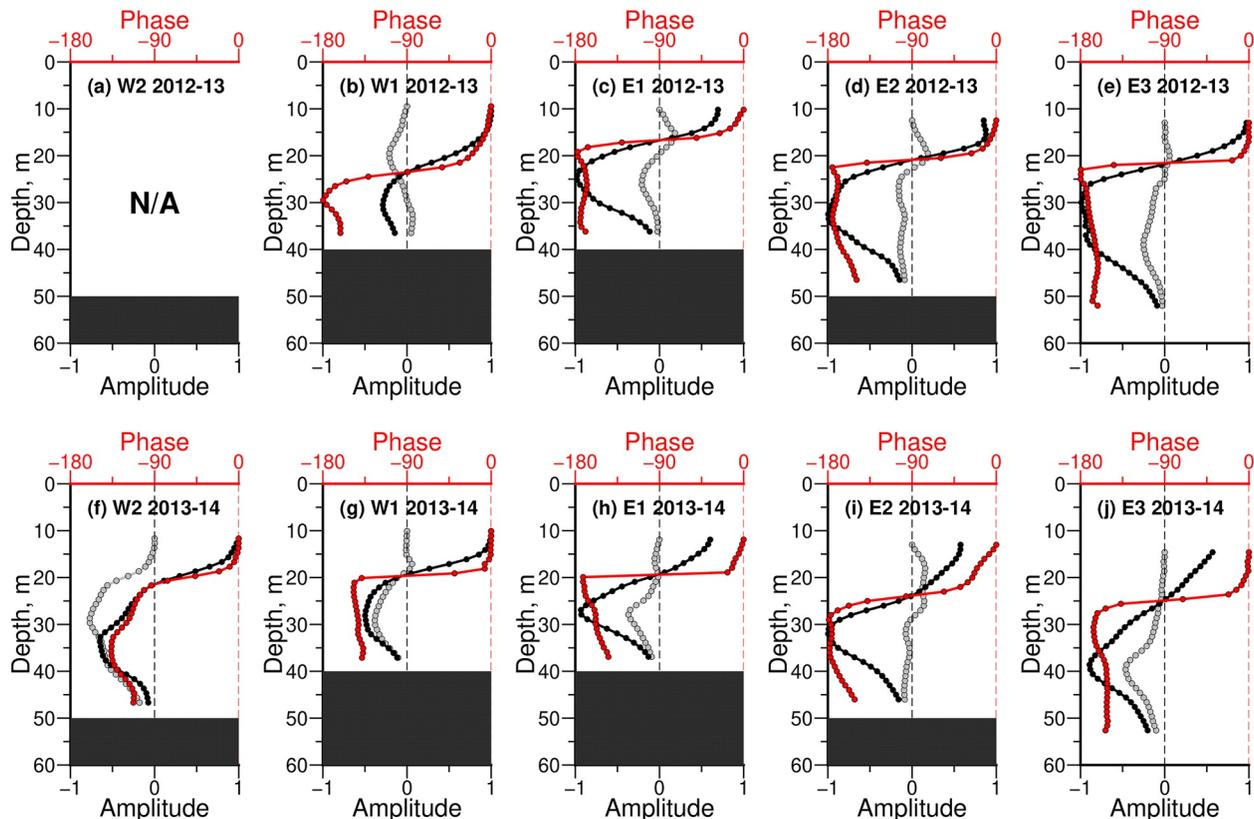
Low sea ice cover

Figure 8. Normalized CEOF Mode-1 eigenfunctions (black: real part; gray: imaginary part) and corresponding phases (red, in unit of degrees) relative to the uppermost bin for the (a)–(e) 2012-13 and (f)–(j) 2013-14 data during the low sea ice cover periods. Data for W2 2012-13 are only available below 25 m and are not suitable for modal decomposition, thus its CEOF mode and phase are not shown.

Table 2

Explained Variances of CEOF Mode-1, CEOF Mode-2, and α, for the Low and High Sea Ice Cover Periods

	LSP (Figure 8)			HSP (Figure 9)		
	Mode–1	Mode–2	α	Mode–1	Mode–2	α
W2 2012-13			N/A			
W1 2012-13	46%	37%	1.2	78%	13%	6.0
E1 2012-13	53%	23%	2.3	71%	13%	5.5
E2 2012-13	58%	18%	3.2	49%	18%	2.7
E3 2013-13	58%	17%	3.4	46%	19%	2.4
W2 2013-14	62%	23%	1.9	92%	5%	18.4
W1 2013-14	52%	33%	1.6	89%	7%	12.7
E1 2013-14	46%	28%	1.8	76%	13%	6.1
E2 2013-14	53%	26%	2.0	21%	23%	2.2
E3 2013-14	51%	24%	2.1	51%	21%	2.4

Note. LSP, low sea ice cover period; HSP, high sea ice cover period.

west. The veering in the BBL coincided with some elevated Mode-1 velocity amplitudes, indicating that velocities are more enhanced within a relatively narrow layer (~10 m) near the bottom (e.g., E1 and E2 in 2012-13, and E1 in 2013-14). This resembles findings of a constrained tidal BBL under stratified conditions by Werner et al. (2003), implying that winter stratification could have an impact on the tides.

The winter CEOF eigenfunctions also show patterns of decreasing velocity amplitudes in the upper water column, although without substantial changes in phase. Morison et al. (1985) demonstrated that an under-ice boundary layer reaches its maximum thickness when the signal frequency (for the case here the semidiurnal tidal frequencies) is close to the local f (see their Figure 4) and has a potential to influence the currents away from the ice boundary. Thus, we assume that the upper layer amplitude decreases seen in the CEOF eigenfunctions could be related to the under-ice boundary layer. For example, Figure 9 shows that the CEOF amplitudes both decreased toward the surface at W1 and E1. However, this decrease is larger in 2013-14 than 2012-13, which could be related to different ice drift speeds and upper-layer currents. Indeed, based on the ADCP-observed sea ice velocities, we find a strong ice drift event (~50 cm s^{-1}) in March 2013 with a larger wind factor of ~0.06–0.08 (Figures 10a and 10b). However, the overall pattern during HSP in terms of the wind factor is less conclusive. Therefore, the strong ice
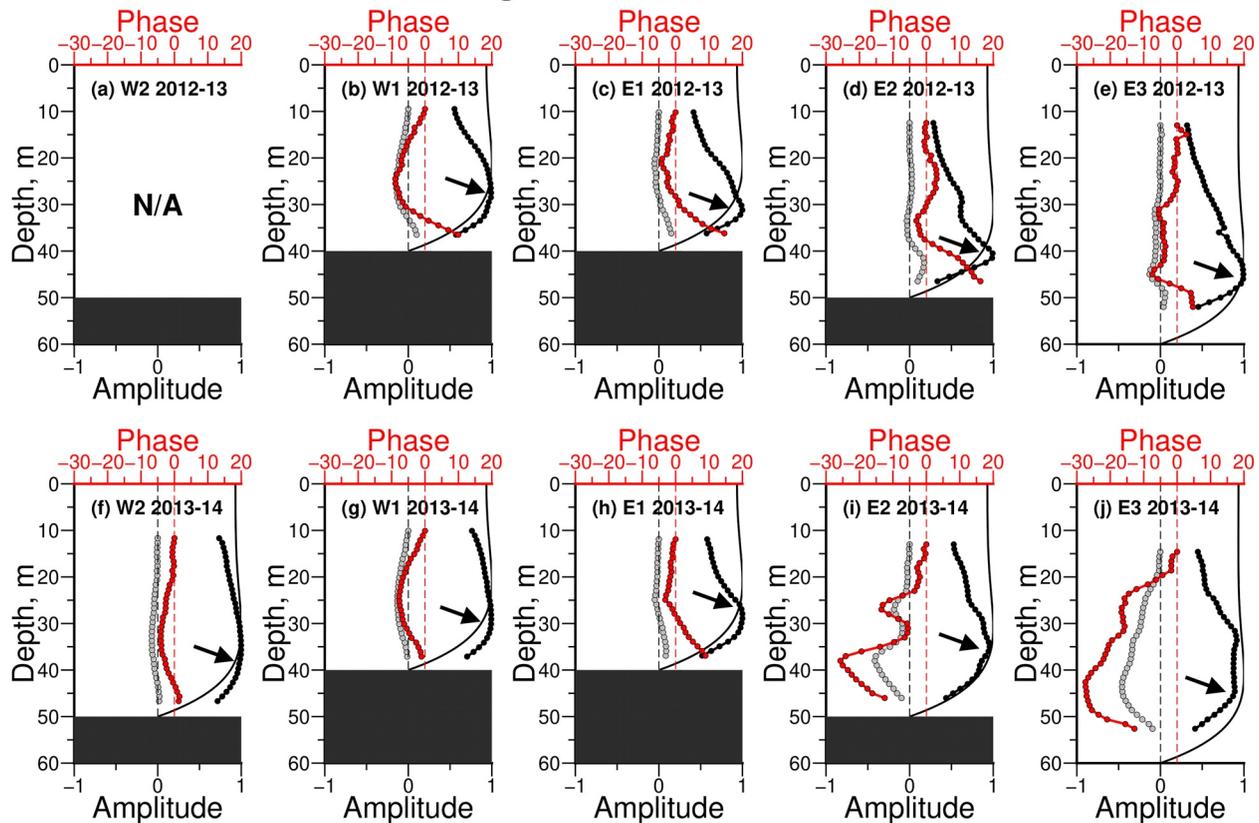
High sea ice cover

Figure 9. Normalized CEOF Mode-1 eigenfunctions (black: real part; gray: imaginary part) and corresponding phases (red, in unit of degrees) relative to the uppermost bin for the (a)–(e) 2012-13 and (f)–(j) 2013-14 data during the high sea ice cover period. Note that the range of phase throughout the water column is much less than for low sea ice cover period (Figure 8). Data for W2 2012-13 are only available below 25 m and are not suitable for modal decomposition, thus its CEOF mode and phase are not shown. Thin black curved lines denote analytical bottom boundary layer (BBL) solutions using Equation 10. Black arrows show the inferred top of the tidal BBL.

drift (and current) event in March 2013 could induce a thicker under-ice boundary layer, which is captured by the CEOF analysis. Detailed observations of the near-surface ocean and sea ice properties are needed to confirm this hypothesis.

For the tide-dominated conditions during HSP, the parameter α (the ratio of CEOF Mode-1 to Mode-2 variances; see above) roughly represents the ratio of barotropic (including the frictional BBL) to baroclinic energy. Larger α indicates that the barotropic tide dominates. Smaller α suggests a larger baroclinic contribution from NIW or internal tides. During HSP the CEOF Mode-1 eigenfunctions at W1 and W2 explain 78%–92% of the total variance, with a large α of ~6–18 (Table 2). While CEOF Mode-2 explains only ~10% of the total variance. On the eastern side, the variance explained by the CEOF Mode-1 eigenfunctions are slightly lower and range from ~21%–50% at E2 and E3 to ~70% at E1, with smaller α compared to the west (Table 2). Total variances explained by the CEOF Mode-2 eigenfunctions yield ~20% at these three eastern sites. The vertical structures of the CEOF Mode-2 eigenfunctions are similar to the Mode-1 eigenfunctions for the LSP (Figure 8) but with a ~10–15 m deeper zero crossing (not shown), implying the existence of a winter pycnocline. Here, the CEOF Mode-2 eigenfunctions may be dominated by episodically-forced NIWs or other band-frequency internal waves, emerging in a more stratified water column on the eastern side of Hanna Shoal. This, in combination with the CEOF patterns shown in Figure 9, implies that the winter stratification east of Hanna Shoal is an important controlling factor on the tides.
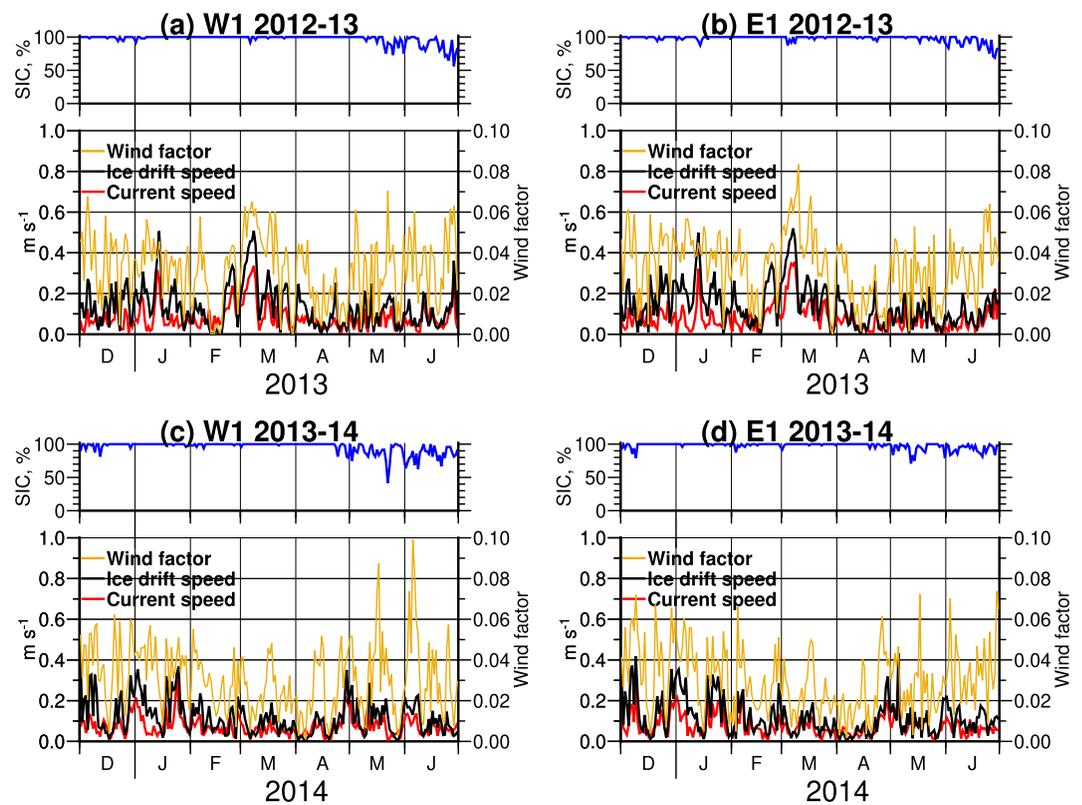
Figure 10. (a) Time series of daily Acoustic Doppler Current Profiler-derived sea ice concentration (blue), ice drift speed (black), and upper-layer ocean current speed (red, from F20) at W1 for the 2012-13 high sea ice cover period. Yellow line is the wind factor. (b) Same as (a), but for E1. (c, d) Same as (a, b), but for the 2013-14 high sea ice period.

3.4. Vertical Distribution of Semidiurnal Energy

The joint effect of NIW and tides on the semidiurnal band during LSP may be viewed in frequency domain. Energy one order of magnitude greater than that at the surrounding frequencies and a vertical structure with two-layered energy peaks appear within the band of $\sim$0.97–1.03 f, with a superinertial tendency concentrated at $\sim$1–1.03 f at some sites (Figure 11). The S_2 and K_2 tides are only seen as a combined signal and cannot be resolved separately in the spectra.

The frequency spectra during HSP (Figure 12) differ significantly from the LSP spectra. The spectral energy during HSP is concentrated at the four dominant semidiurnal tidal frequencies rather than at $\sim$$f$, showing that the semidiurnal energy is primarily derived from tides (Figure 12). The dominant M_2 tide has an energy level that is $\sim$4–6 times greater than the other three semidiurnal constituents at W1 and W2 for the 2012-13 (Figures 12a and 12b) and 2013-14 (Figures 12f and 12g) records, in particular in the lower part of the water column. This indicates an enhanced barotropic M_2 BBL near the critical latitude, consistent with the CEOF results (e.g., Figure 9).

The eastern spectra exhibit a different pattern compared to W1 and W2 (Figures 12c–12e and Figures 12h–12j). For the 2012-13 record, bottom-enhanced tidal energy is seen at E1 and E2, with a second energy peak emerging between 18–30 m depth at E3 (Figures 12c–12e). Moreover, both deployments reveal lower vertical extents of the tidal energy (i.e., W2 vs. E2, W1 vs. E1) including smaller tidal BBLs in the east. The pattern is less obvious at E3 but, overall, the eastern frequency spectra in Figure 12 indicate greater energy in the lower part of the water column, in contrast to the depth-independent energy distribution in the western records. These results may further explain the more variable correlations and larger error bars between the monthly $t_m(z)$ and t_{AOTIM} in winter east of Hanna Shoal (Figure 2). Overall, the CEOF and spectral analyses indicate an east-west asymmetry of semi-diurnal tides around Hanna Shoal underlined by more confined tidal BBLs due to winter stratification east of
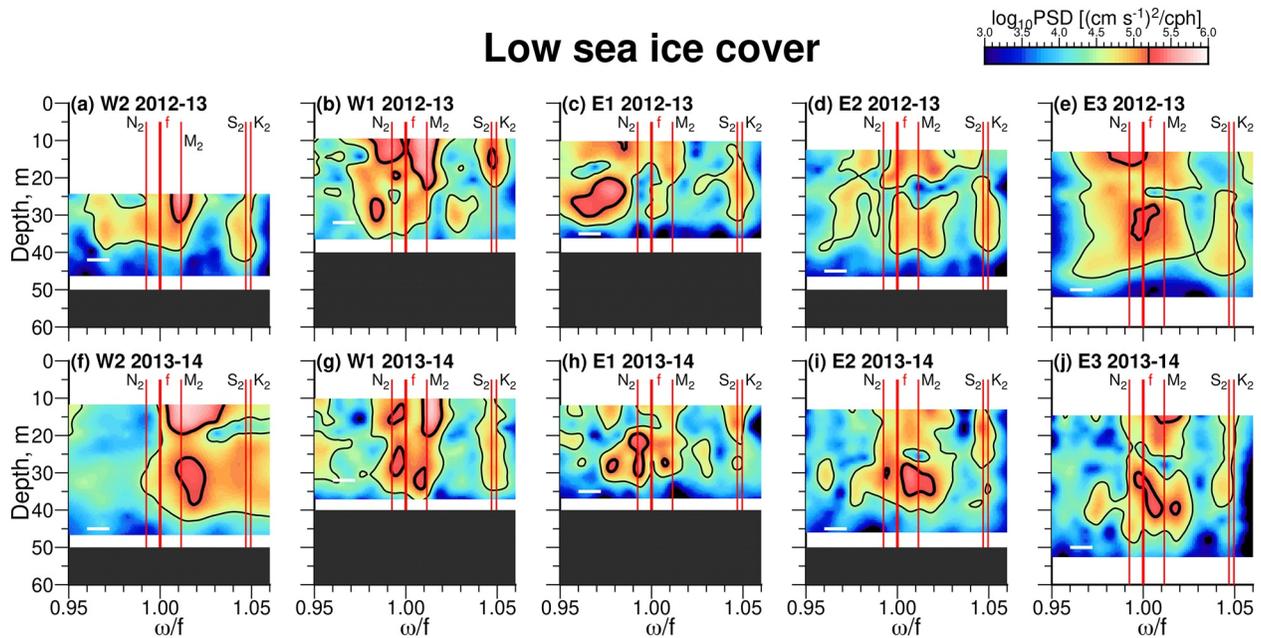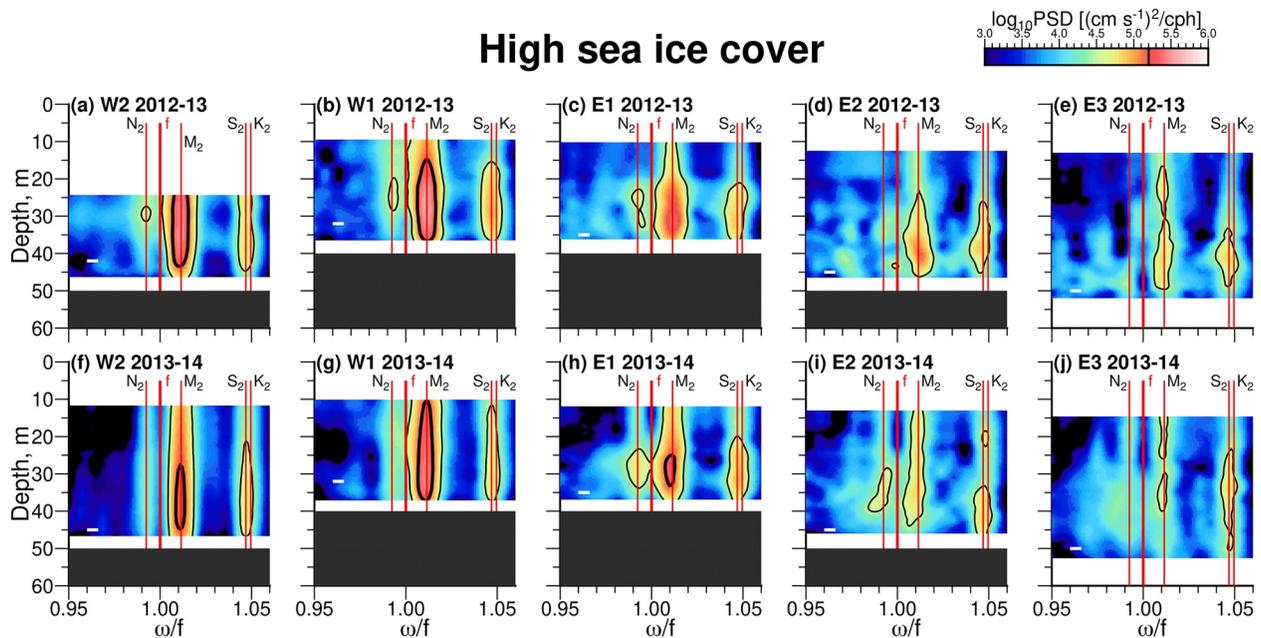
Figure 11. Depth-frequency colored contours of clockwise spectra (as power spectral density, PSD, in $(cm\ s^{-1})^2/cph$) for all five moorings during the low sea ice cover period in (a)–(e) 2012-13 and (f)–(j) 2013-14. Frequency is normalized with the local f. The thick red line denotes the local f, and the other four red lines (from left to right) denote the frequencies of the N_2, M_2, S_2, and K_2 semidiurnal tides. Horizontal white bars denote the spectral resolution. Thin and thick black contours denote the $\log_{10}(PSD)$ levels of 4.5 and 5.2, respectively.

Figure 12. Depth-frequency colored contours of clockwise spectra (as power spectral density, PSD, in $(cm\ s^{-1})^2/cph$) for all five moorings during the high sea ice cover period in (a)–(e) 2012-13 and (f)–(j) 2013-14. Frequency is normalized with the local f. The thick red line denotes the local f, and the other four red lines (from left to right) denote the frequencies of the N_2, M_2, S_2, and K_2 semidiurnal tides. Horizontal white bars denote the spectral resolution. Thin and thick black contours denote the $\log_{10}(PSD)$ levels of 4.5 and 5.2, respectively.

Hanna Shoal (Figure 12). The reduced tidal BBL height results in a velocity maximum close to the bottom with strongly sheared flows (e.g., Figure 6), which is consistent with other observations on shallow shelves (e.g., Maas & Van Haren, 1987; Werner et al., 2003).

4. Discussion

4.1. Tide-Driven Shear

Our observations show that tides dominate the semidiurnal variability during consolidated sea ice cover periods (HSPs) and, more importantly, significant baroclinic tidal energy is present east of Hanna Shoal, where the resultant tidal BBL is thinner due to effects of stratification. We calculate velocity shear squared, $S_{sq}^2 = (\partial u/\partial z)^2 + (\partial v/\partial z)^2$, as a potential indicator for tide-driven mixing by first-differencing the band-passed 1-m-binned ADCP velocities (Figure 13). We examined various depth ranges (2, 5, 10, and 15 m) for the shear computation and found that S_{sq}^2 computed from small depth ranges (<5 m) exhibited semidiurnal fluctuations. Semidiurnally-amplified near-bottom currents ($\sim$10–15 cm s^{-1}) were found in the lower layer (>30 m) under weak winds and ice drift (>90% SIC) (e.g., Figure 10), as manifested by large S_{sq}^2 values (>10×10^{-4} s^{-2}) during late-May of 2013 at E2 and E3 (Figures 13d and 13e). Patterns of amplified near-bottom S_{sq}^2 similar to those shown in Figure 12 were also observed in late January 2013 under comparable conditions with weak winds and $\sim$100% SIC (Figure S1 in Supporting Information S1). We had examined these shear data in detail by performing a rotational separation of shear vector components following Halle and Pinkel (2003, see their Section 3.2). The results (Figure S2 in Supporting Information S1) point out that the shear was dominated by the CW component and indicate that surface-forced NIW are likely not the driver for the strong shear event shown in Figure 13. It is possible that the observed near-bottom event of exceptionally high shear during 22 May–29 May (we call it the shear event later) at E2 and, especially, E3 was tidally-forced as this time period coincided with the spring tide (see u-component of t_{AOTIM} shown in Figure 13).

To examine the potential of the tide-driven shear in late May 2013 to reduce lower water column stability and trigger mixing, we computed a crude estimate of the lower-layer stratification during this period by using density differences between the available mid-depth and near-bottom CTD sensors at E2 and E3 (Figure 14c):

$$N^2 \approx -\frac{g}{\rho_0} \left(\frac{\Delta \rho}{\Delta z} \Big|_{z=near-bottom}^{z=mid-depth} \right), \tag{12}$$

We assume the estimated N^2 here can be also applied to the depth range of the tide-driven shear. Note that the vertical separation ($\sim$20 m) of the CTD sensors at E2 and E3 (e.g., see two horizontal lines in Figure 13) was larger than the vertical extent ($\sim$10 m) of the tide-driven shear. Thus, there was no apparent change in temperature and salinity during the shear event (the time period of the event is marked in Figure 14a) at mid-depth. Comparing the near-bottom conditions between east and west, we see a slight warming and freshening at E2 after 22 May (Figure 14a). We computed an estimate of the shear squared in the lower-layer, $<S_{sq}^2>$, evaluated as a vertical average for a 10-m thick layer from the lowest bin at E2 and E3. The results shows that $<S_{sq}^2>$ were amplified 2–5 times during the shear event (Figure 14d). To examine the water column stability we use Equation 12 and yield a bulk Richardson number, $N^2/<S_{sq}^2>$, of the lower-layer. The analysis highlights reduced bulk Richardson numbers to below 1 during the shear event, and in particular to the critical level of $\sim$0.25 during 24–25 May (Figure 14e). These numbers during this shear event are comparable with other observation-based Richardson numbers (e.g., D'Asaro, 1985b; Evans, 1982) and suggest favorable conditions for shear instability to occur (e.g., Cushman-Roisin & Beckers, 2011). These results underline that the tide-driven shear could be capable of stirring the lower water column in winter, implying that internal tides could potentially contribute to lower-layer diapycnal mixing east of Hanna Shoal when the ocean is covered by sea ice.

Recent studies associated local productivity with the annual arrival of WW around the Hanna Shoal region (Danielson et al., 2017; Lin et al., 2019; Lowry et al., 2015), but the physical mechanisms required to flux WW-nutrients toward the sunlit upper ocean have not been previously documented. Here, we propose that once the annual arrival of nutrient-rich WW has reached the eastern Hanna Shoal region, dynamic instabilities initiated by tide-driven shear (e.g., Figure 14e) may provide a mechanism to transport these WW nutrients into the euphotic layer during the early summer sea ice breakup. Although our observations lack the vertical resolution
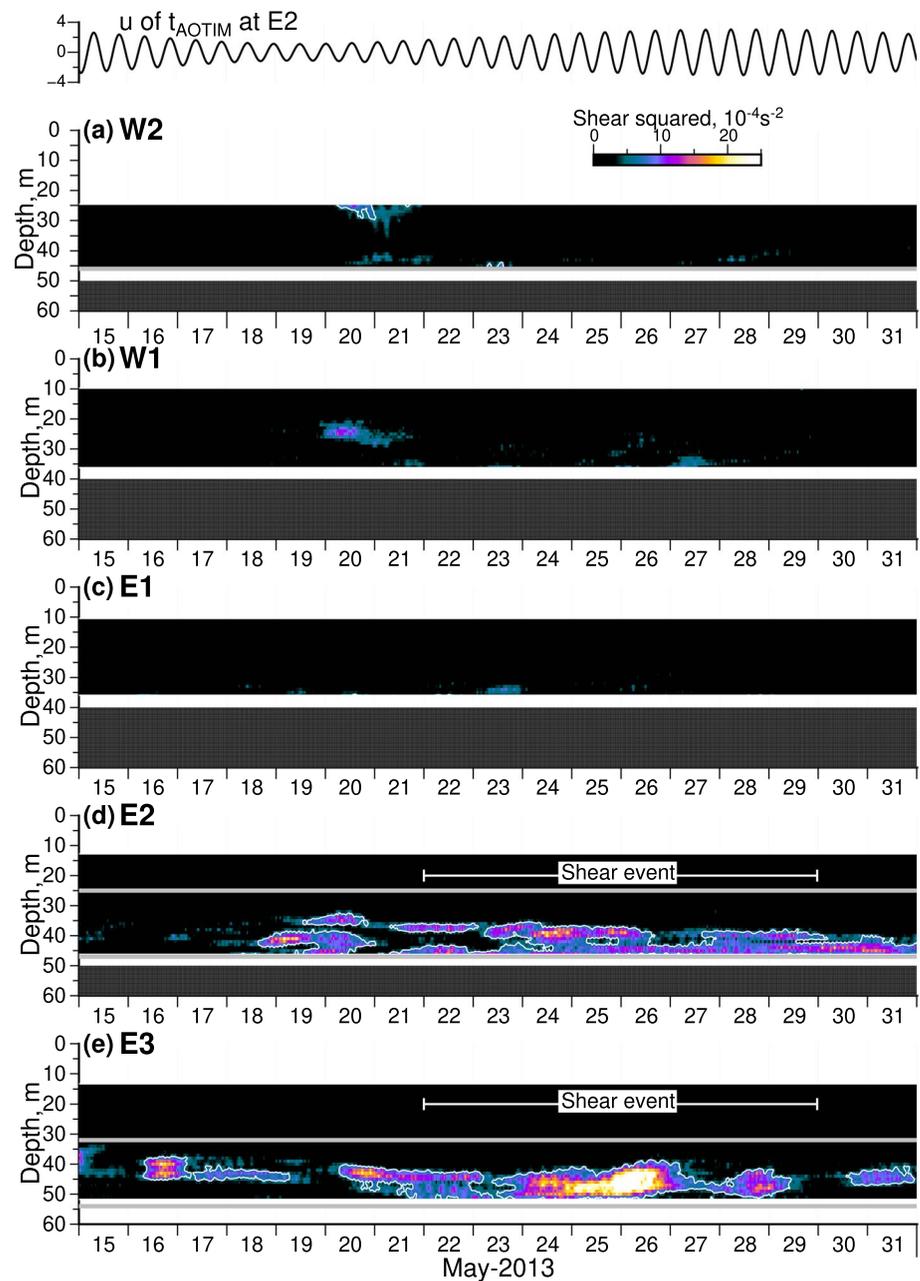
Figure 13. Band-passed shear-squared of the observed currents (colored shading) for 15–31 May 2013 (in a period of high sea ice concentration, see Figure 10) at each mooring. White contours denote the level of $10 \times 10^{-4} \text{ s}^{-2}$. The black line at the top of (a) shows the u-component of t_{AOTIM} (black, in unit of cm s^{-1}) at E2. Gray horizontal lines at (a), (d), and (e) denote the depths of the Conductivity-Temperature-Depth sensors. The time period of the shear event (see text) is labeled in (d) and (e).

needed to quantify stratification and to more reliably infer vertical mixing, our analyses provide indications that tidal mixing east of Hanna Shoal should be considered as a potential mechanism to replenish nutrients in addition to convective mixing in winter (e.g., Arrigo et al., 2017; Lowry et al., 2018).

4.2. Possible Generation Sites for the Semidiurnal Internal Tides

Our data show that semidiurnal internal tides east of Hanna Shoal during HSP appear unrelated to the fortnightly cycle (Figure 6), and may thus be generated remotely by the interaction between enhanced currents during flood or ebb tides, bathymetry, and stratification. Another generation mechanism may result from the interaction of the
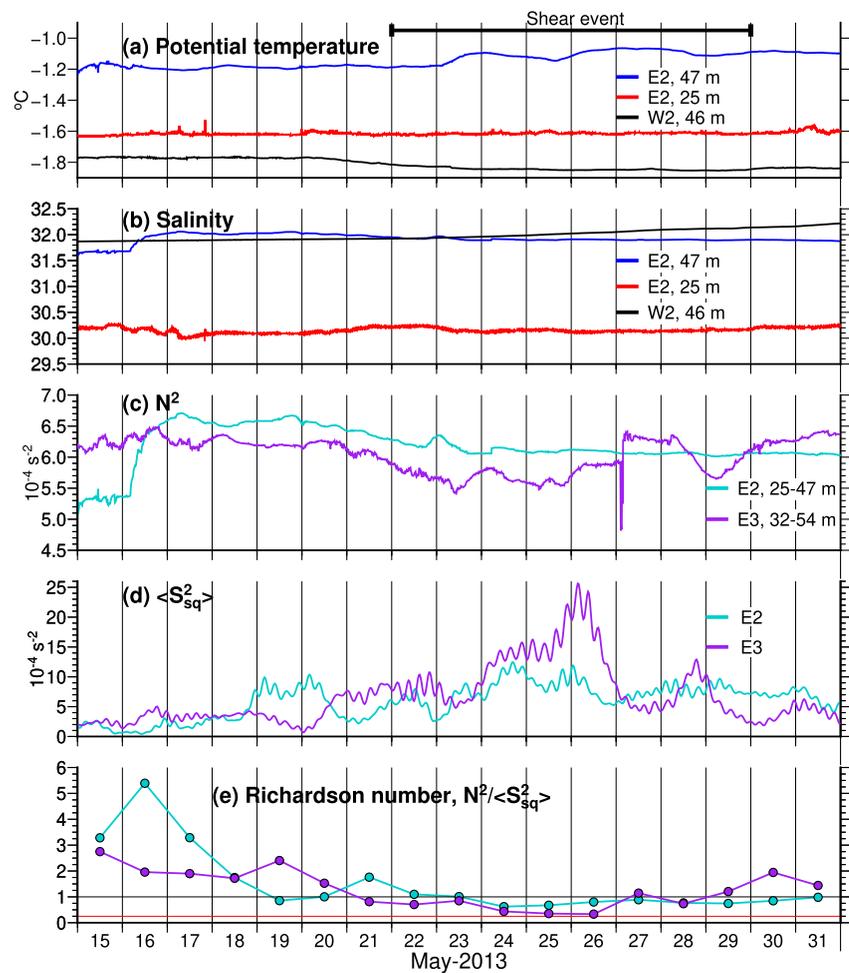
Figure 14. (a) Time series of potential temperature at 25 m (red) and 47 m (blue) depth at E2, and at 46 m at W2 (black) during 15 May–31 May 2013. (b) Same as (a), but for salinity. (c) Time series of estimated lower-layer buoyancy-frequency-squared (N^2) based on Equation 12 from the available Conductivity-Temperature-Depth sensors at mid-depth and near-bottom at E2 (cyan) and E3 (purple). (d) Vertically-averaged shear squared, $<S_{sq}^2>$, evaluated for a 10-m thick layer from the lowest bin at E2 (cyan) and E3 (purple). (e) Estimated daily lower-layer Richardson number by $N^2/<S_{sq}^2>$ at E2 (cyan) and E3 (purple). Critical levels of 1 and 0.25 are highlighted by horizontal black and red lines, respectively. The time period of the shear event shown in Figure 13 is marked in (a).

CW-rotating barotropic tide with the bottom topography of Hanna Shoal. This interaction could eventually result in freely propagating internal waves with semidiurnal frequency (e.g., Wunsch, 1975), as the mooring sites were still south of the critical latitude (Figure 1a). These options are further investigated by use of the co-tidal charts of the M_2 amplitude and the Greenwich phase lag derived from the AOTIM-5 barotropic tidal model (Figure 15). The results indicate that tidal waves propagate southeastward from the Arctic Basin toward the Chukchi shelf. The barotropic semidiurnal tide is then guided by the local bathymetry with the tidal phase at W2 leading that at E2 about ~20° (equivalent to ~1.3 hr). The amplitude of the barotropic semidiurnal tide somewhat decreases from ~2.75 cm at W2 to ~2.5 cm at E2. This suggests that the barotropic tide has a broad and coherent footprint around Hanna Shoal. However, our observations yield very different patterns where the tides west of Hanna Shoal clearly follow the spring-neap tidal phase, whereas this is not the case in the east (e.g., Figures 6 and 13).

To investigate possible generation sites of observed internal tides, we followed the velocity hodograph methods (a representation of current ellipses) of Alford and Zhao (2007) and Zhao et al. (2010) by creating monthly hodographs derived from wintertime band-passed u and v components. Our computed hodographs (not shown) are highly variable in time and are characterized by near-circular patterns, rather than a particular orientation suggesting internal tide propagation direction. We therefore compare the local topographic slopes, s, around
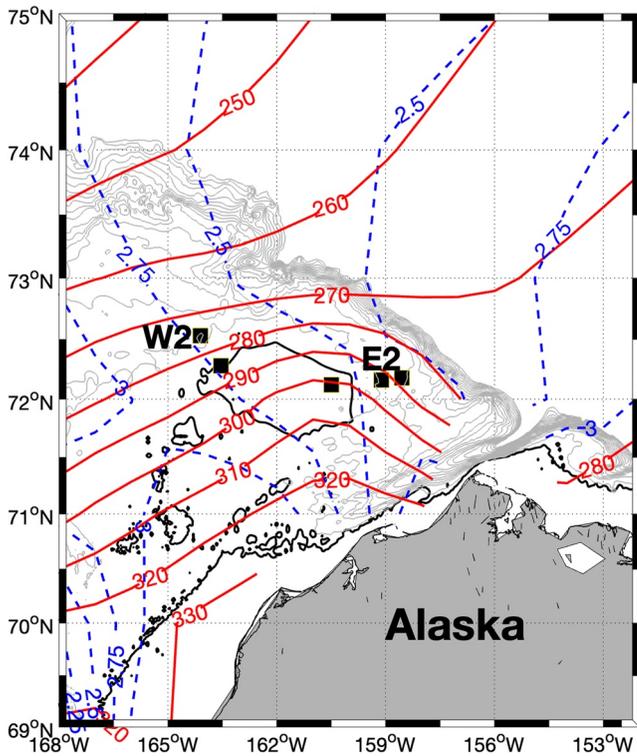
Figure 15. Co-tidal lines of amplitude (elevation in cm, blue dashed lines) and Greenwich phase lag (in unit of degrees, solid red lines) of the M_2 tide from the AOTIM-5 barotropic tidal model in the Hanna Shoal region. Thick black contours denote the 40-m isobath. Gray contours denote isobaths from 50–200 m depths at 10-m intervals. Black squares are mooring locations.

Hanna Shoal with the theoretical internal wave characteristic slope, γ, at the M_2 frequency (e.g., Park & Watts, 2006) and near-bottom N^2, using

$$\gamma = \pm \left(\frac{\omega_{M_2}^2 - f^2}{N^2 - \omega_{M_2}^2} \right)^{1/2}, \quad (13)$$

We define seven transects around Hanna Shoal and divide these into shelf and shelfbreak (and Barrow Canyon) segments (Figure 16a). Favorable topographic conditions for internal tide generation based on linear generation models (e.g., Baines, 1973) are assumed where s is close to γ. The topographic slopes along each of the transects are calculated as follows. First, a slope s_t for a length of every 10 km along a transect is calculated, then a median of the collected s_t is retrieved as the representative s for the transect. We further separated the shelf and shelfbreak transects in this stage by observing the sharp change of s_t. When γ is plotted as a function of a varying near-bottom N^2, Figure 16b for instance shows that s of Line 7 equals γ (favorable for internal tide generation) when $N^2 = \sim 2 \times 10^{-4}$ s^{-2}.

For the shelf transects s ranges from ~ 0.6–2.9×10^{-4}, whereas the shelfbreak and Barrow Canyon transects (except Line 4-1) reveal much steeper values of s on the order of ~ 11–50×10^{-4} (Figure 16b), and are thus excluded from further discussions. Using the crude estimate of near-bottom N^2 from Figure 14c, we may reasonably assume an N^2 of $\sim < 10 \times 10^{-4}$ s^{-2} about 20 m above the bottom (Figure 16b). Based on Figure 16b, potential regions with bottom topography (e.g., $s = \sim \gamma$) favorable for internal tide generation span the northern half of Hanna Shoal. We note that γ will decrease as near-bottom N^2 increases (Figure 16b); for example, γ will reduce from $\sim 0.75 \times 10^{-4}$ to $\sim 0.4 \times 10^{-4}$ (i.e., regions near Line 1) if near-bottom N^2 increases from 20×10^{-4} to 80×10^{-4} s^{-2}. However, except for regions near Lines 5 and 6 spanning the southeastern and eastern flanks of Hanna Shoal, we suspect there exists persistent stratification in other places. Our analysis thus indicates that the events with enhanced near-bottom shear we observed at the eastern moorings (Figure 13) are likely manifestations of internal tides generated near the southeastern and eastern flanks of Hanna Shoal (see red lines in Figure 16a) in response to local bathymetry and winter stratification.
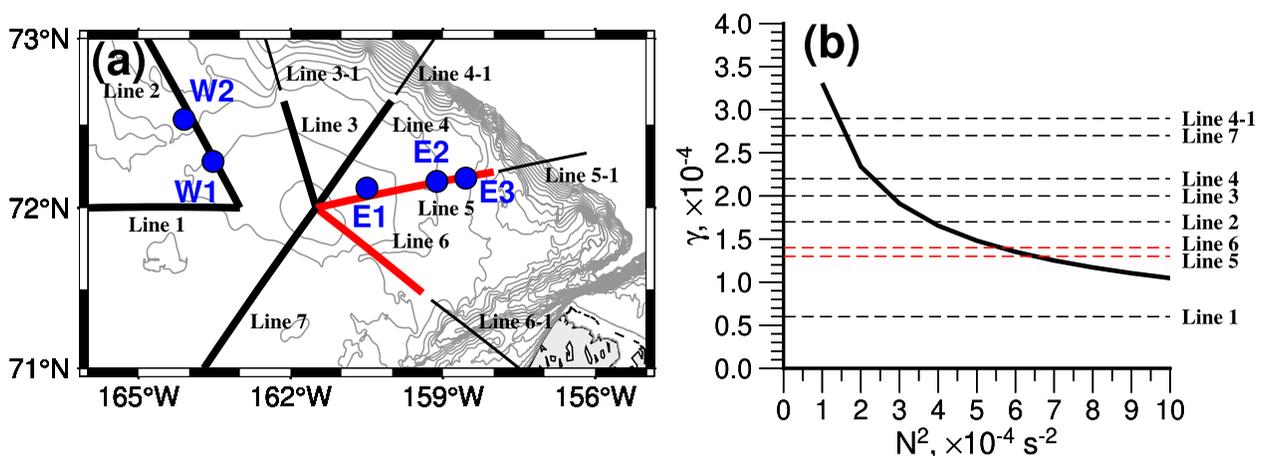

Figure 16. (a) Selected transects (black lines) for topographic slope calculations. Thicker lines denote shelf transects (Lines 1–7), whereas thinner lines denote shelfbreak (Lines 3-1, 4-1, and 5-1) and Barrow Canyon (Line 6-1) transects. Gray lines are bathymetric contours at 10-m intervals for 10–200 m. (b) The theoretical internal wave characteristic slope γ with the M_2 frequency as a function of assumed winter near-bottom N^2 based on Equation 13. Topographic slopes from selected transects are listed on the right of the figure. Red lines shown in (a) and red dashed lines in (b) highlight potential transects where the topographic slopes favor internal tide generation. For example, Lines 5 and 6 are favorable for internal tide generation when near-bottom N^2 is $\sim 6 \times 10^{-4}$ s^{-2}.

5. Summary and Conclusions

We used velocity observations derived from five bottom-mounted upward-looking ADCP moorings to investigate the role of semidiurnal tides and their seasonal variability on the ocean dynamics around Hanna Shoal. The records span two full years, allowing us to examine water column structure and internal processes related to semidiurnal tides underneath a fully developed sea ice cover. Our analyses and results indicate seasonal and regional differences in the semidiurnal tidal structure around Hanna Shoal, which has the following implications:

1. The semidiurnal variability of the Hanna Shoal region has a strong seasonality, characterized by surface-forced NIWs during ice-free or weakly ice-covered periods, while the tides prevail during the high sea ice cover periods.
2. During high sea ice cover periods, semidiurnal tides are primarily barotropic characterized by tidal BBL with a thickness of about 30%–50% of the water depth on the western flank of Hanna Shoal, whereas the tides display a baroclinic structure in deeper regions along the eastern flank of the shoal. A unique signature is the bottom-trapped tidal BB, an indication for the tides in response to the year-round persistent stratification east of Hanna Shoal.
3. Episodic tide-driven shear east of Hanna Shoal during the high sea ice cover periods may be sufficiently strong relative to the local stratification. This tide-driven shear can potentially lead to near-bottom conditions with Richardson numbers below 1, and even as low as 0.25. This is expected to create turbulent mixing due to shear instability that erodes the lower water column stability and thus allows water exchange between the upper and lower water column. Recent studies have indicated that the annual arrival of nutrient-rich WW is critical for the Hanna Shoal ecosystem, and tide-induced vertical mixing may support enhanced under-ice phytoplankton growth during the early summer breakup.
4. The southeastern and eastern flanks of Hanna Shoal may be favorable for generating semidiurnal internal tides. Our analyses indicate that such internal tides are generated by the barotropic tides interacting with the local bathymetry and stratification.

Our results suggest that the notion of a quiescent oceanic interior in the Chukchi Sea region, once wind mixing is hampered by sea ice, does not apply to the entire Chukchi Sea shelf. Persistent stratification fundamentally affects both the background circulation and tidal characteristics. This study shows that internal waves at the tidal frequency appear at some portion of the Chukchi Sea shelf, raising the question of where and how this internal wave energy is dissipated. A solid understanding of the processes discussed in this paper relies on a quantitative understanding of the ocean's stratification. This is admittedly poor due to low vertical resolution and lacking upper ocean sensors in our data sets, as is the case for most mooring records in ice-covered regions, and future ecosystem studies would benefit from full-water-column mooring designs.

Data Availability Statement

NCEP Reanalysis data was obtained from the NOAA/OAR/ ESRL PSD, Boulder, CO, USA, and is available at the website: https://psl.noaa.gov/data/gridded/data.narr.monolevel.html. The COMIDA mooring and moored CTD data are available at NODC via https://www.nodc.noaa.gov/archive/arc0109/0163833/ and a netCDF version is recently archived at the Arctic Data Center via http://doi.org/10.18739/A25M6280M. Please note that the original names of the COMIDA moorings were different from those used in this paper. Readers may refer to Table 1 of Fang et al. (2020). The COMIDA shipboard hydrographic data are available via http://www.arcticstudies.org/hannashoal/data.html.

References

Alford, M. H., MacKinnon, J. A., Simmons, H. L., & Nash, J. D. (2016). Near-inertial internal gravity waves in the ocean. *Annual Review of Marine Science*, *8*(1), 95–123. https://doi.org/10.1146/annurev-marine-010814-015746

Alford, M. H., & Zhao, Z. (2007). Global patterns of low-mode internal-wave propagation. Part I: Energy and energy flux. *Journal of Physical Oceanography*, *37*(7), 1829–1848. https://doi.org/10.1175/JPO3085.1

Arrigo, K. R., Mills, M. M., van Dijken, G. L., Lowry, K. E., Pickart, R. S., & Schlitzer, R. (2017). Late spring nitrate distributions beneath the ice-covered northeastern Chukchi Shelf. *Journal of Geophysical Research: Biogeosciences*, *122*(9), 2409–2417. https://doi.org/10.1002/2017JG003881

Baines, P. G. (1973). The generation of internal tides by flat-bump topography. *Deep-Sea Research and Oceanographic Abstracts*, *20*(2), 179–205. https://doi.org/10.1016/0011-7471(73)90050-8

Baumann, T. M., Polyakov, I. V., Padman, L., Danielson, S., Fer, I., Janout, M., et al. (2020). Arctic tidal current atlas. *Scientific Data*, *7*(1), 1–11. https://doi.org/10.1038/s41597-020-00578-z

Blanchard, A. L., Day, R. H., Gall, A. E., Aerts, L. A. M., Delarue, J., Dobbins, E. L., et al. (2017). Ecosystem variability in the offshore northeastern Chukchi Sea. *Progress in Oceanography*, *159*, 130–153. https://doi.org/10.1016/j.pocean.2017.08.008

Corlett, W. B., & Pickart, R. S. (2017). The Chukchi slope current. *Progress in Oceanography*, *153*, 50–65. https://doi.org/10.1016/j.pocean.2017.04.005

Cushman-Roisin, B., & Beckers, J.-M. (2011). Chapter 14—Turbulence in stratified fluids. In B. Cushman-Roisin & J. M. Beckers (Eds.), *Introduction to geophysical fluid dynamics: Physical and numerical aspects* (Vol. 101, pp. 425–470). Academic Press. https://doi.org/10.1016/B978-0-12-088759-0.00014-6

Danielson, S. L., Eisner, L., Ladd, C., Mordy, C., Sousa, L., & Weingartner, T. J. (2017). A comparison between late summer 2012 and 2013 water masses, macronutrients, and phytoplankton standing crops in the northern Bering and Chukchi Seas. *Deep Sea Research Part II: Topical Studies in Oceanography*, *135*, 7–26. https://doi.org/10.1016/j.dsr2.2016.05.024

Danielson, S. L., & Kowalik, Z. (2005). Tidal currents in the St. Lawrence Island region. *Journal of Geophysical Research*, *110*(10), 1–18. https://doi.org/10.1029/2004JC002463

D'Asaro, E. A. (1985a). The energy flux from the wind to near-inertial motions in the surface mixed layer. *Journal of Physical Oceanography*, *15*(8), 1043–1059. https://doi.org/10.1175/1520-0485(1985)015<1043:TEFFTW>2.0.CO;2

D'Asaro, E. A. (1985b). Upper Ocean temperature structure, inertial currents, and Richardson numbers observed during strong meteorological forcing. *Journal of Physical Oceanography*, *15*(7), 943–962. https://doi.org/10.1175/1520-0485(1985)015<0943:UOTSIC>2.0.CO;2

D'Asaro, E. A., Eriksen, C. C., Levine, M. D., Paulson, C. A., Niiler, P., & Van Meurs, P. (1995). Upper-ocean inertial currents forced by a strong storm. Part I: Data and comparisons with linear theory. *Journal of Physical Oceanography*, *25*(11), 2909–2936. https://doi.org/10.1175/1520-0485(1995)025<2909:UOICFB>2.0.CO;2

de La Lama, M. S., LaCasce, J. H., & Fuhr, H. K. (2016). The vertical structure of ocean eddies. In *Dynamics and Statistics of the Climate System* (p. dzw001). https://doi.org/10.1093/climsys/dzw001

Dunton, K. H., Ashjian, C., Campbell, R. G., Cooper, L. W., Grebmeier, J. M., Harvey, H. R., et al. (2016). Chukchi Sea offshore monitoring in drilling area (COMIDA): Hanna Shoal ecosystem study. Final report. Retrieved from http://arcticstudies.org/hannashoal/doc/COMIDA%20HS%20Final%20Report%20Aug%202016.pdf

Dunton, K. H., Grebmeier, J. M., & Trefry, J. H. (2017). Hanna Shoal: An integrative study of a High Arctic marine ecosystem in the Chukchi Sea. *Deep Sea Research Part II: Topical Studies in Oceanography*, *144*, 1–5. https://doi.org/10.1016/j.dsr2.2017.09.001

Edwards, C. R., & Seim, H. E. (2008). Complex EOF analysis as a method to separate barotropic and baroclinic velocity structure in shallow water. *Journal of Atmospheric and Oceanic Technology*, *25*(5), 808–821. https://doi.org/10.1175/2007JTECHO562.1

Emery, W. J., & Thomson, R. E. (1997). *Data analysis methods in physical oceanography*. Pergamon.

Erofeeva, S., & Egbert, G. (2020). *Arc5km2018: Arctic Ocean inverse tide model on a 5 kilometer grid, 2018*. Arctic Data Center. https://doi.org/10.18739/A21R6N14K

Evans, D. L. (1982). Observations of small-scale shear and density structure in the ocean. *Deep-Sea Research, Part A: Oceanographic Research Papers*, *29*(5), 581–595. https://doi.org/10.1016/0198-0149(82)90077-2

Fang, Y.-C., Potter, R. A., Statscewich, H., Weingartner, T. J., Winsor, P., & Irving, B. K. (2017). Surface current patterns in the northeastern Chukchi Sea and their response to wind forcing. *Journal of Geophysical Research: Oceans*, *122*(12), 9530–9547. https://doi.org/10.1002/2017JC013121

Fang, Y.-C., Weingartner, T. J., Dobbins, E. L., Winsor, P., Statscewich, H., Potter, R. A., et al. (2020). Circulation and thermohaline variability of the Hanna Shoal region on the northeastern Chukchi Sea shelf. *Journal of Geophysical Research: Oceans*, *125*(7), e2019JC015639. https://doi.org/10.1029/2019JC015639

Fer, I. (2014). Near-inertial mixing in the central Arctic Ocean. *Journal of Physical Oceanography*, *44*(8), 2031–2049. https://doi.org/10.1175/JPO-D-13-0133.1

Foreman, M. G. G. (1977). *Manual for tidal heights analysis and prediction. Pacific Marine Science Report 77-10*. Institute of Ocean Sciences.

Furevik, T., & Foldvik, A. (1996). Stability at M2 critical latitude in the Barents Sea. *Journal of Geophysical Research*, *101*(C4), 8823–8837. https://doi.org/10.1029/96JC00081

Gonella, J. (1972). A rotary-component method for analysing meteorological and oceanographic vector time series. *Deep-Sea Research and Oceanographic Abstracts*, *19*(12), 833–846. https://doi.org/10.1016/0011-7471(72)90002-2

Gong, D., & Pickart, R. S. (2015). Summertime circulation in the eastern Chukchi Sea. *Deep Sea Research Part II: Topical Studies in Oceanography*, *118*, 18–31. https://doi.org/10.1016/j.dsr2.2015.02.006

Grebmeier, J. M., Bluhm, B. A., Cooper, L. W., Danielson, S. L., Arrigo, K. R., Blanchard, A. L., et al. (2015). Ecosystem characteristics and processes facilitating persistent macrobenthic biomass hotspots and associated benthivory in the Pacific Arctic. *Progress in Oceanography*, *136*, 92–114. https://doi.org/10.1016/j.pocean.2015.05.006

Grebmeier, J. M., Cooper, L. W., Feder, H. M., & Sirenko, B. I. (2006). Ecosystem dynamics of the Pacific-influenced northern Bering and Chukchi Seas in the Amerasian Arctic. *Progress in Oceanography*, *71*(2–4), 331–361. https://doi.org/10.1016/j.pocean.2006.10.001

Halle, C., & Pinkel, R. (2003). Internal wave variability in the Beaufort Sea during the winter of 1993/1994. *Journal of Geophysical Research*, *108*(C7), 3210. https://doi.org/10.1029/2000JC000703

Hibler, W. D. (1979). A dynamic thermodynamic sea ice model. *Journal of Physical Oceanography*, *9*(4), 815–846. https://doi.org/10.1175/1520-0485(1979)009<0815:ADTSIM>2.0.CO;2

Howard, S. L., & Padman, L. (2021). *Arc2kmTM: Arctic 2 kilometer tide model, 2021*. Arctic Data Center. https://doi.org/10.18739/A2PV6B79W

Itoh, M., Nishino, S., Kawaguchi, Y., & Kikuchi, T. (2013). Barrow Canyon volume, heat, and freshwater fluxes revealed by long-term mooring observations between 2000 and 2008. *Journal of Geophysical Research: Oceans*, *118*(9), 4363–4379. https://doi.org/10.1002/jgrc.20290

Janout, M. A., & Lenn, Y.-D. (2014). Semidiurnal tides on the Laptev Sea shelf with implications for shear and vertical mixing. *Journal of Physical Oceanography*, *44*(1), 202–219. https://doi.org/10.1175/jpo-d-12-0240.1

Kaihatu, J. M., Handler, R. A., Marmorino, G. O., & Shay, L. K. (1998). Empirical orthogonal function analysis of ocean surface currents using complex and real-vector methods. *Journal of Atmospheric and Oceanic Technology*, *15*(4), 927–941. https://doi.org/10.1175/1520-0426(1998)015<0927:eofaoo>2.0.co;2

Kara, A. B., Wallcraft, A. J., Metzger, E. J., Hurlburt, H. E., & Fairall, C. W. (2007). Wind stress drag coefficient over the global ocean. *Journal of Climate*, *20*(23), 5856–5864. https://doi.org/10.1175/2007JCLI1825.1

Kawaguchi, Y., Itoh, M., Fukamachi, Y., Moriya, E., Onodera, J., Kikuchi, T., & Harada, N. (2019). Year-round observations of sea-ice drift and near-inertial internal waves in the Northwind Abyssal Plain, Arctic Ocean. *Polar Science*, *21*, 212–223. https://doi.org/10.1016/j.polar.2019.01.004

Kundu, P. K. (1976). Ekman veering observed near the ocean bottom. *Journal of Physical Oceanography*, *6*(2), 238–242. https://doi.org/10.1175/1520-0485(1976)006<0238:EVONTO>2.0.CO;2

Kundu, P. K., Cohen, I. M., & Dowling, D. R. (Eds.) (2012). *Chapter 13—Geophysical fluid dynamics* (pp. 621–690). Academic Press. https://doi.org/10.1016/B978-0-12-382100-3.10013-7

Kunze, E. (1985). Near-inertial wave propagation in geostrophic shear. *Journal of Physical Oceanography*, *15*(5), 544–565. https://doi.org/10.1175/1520-0485(1985)015<0544:NIWPIG>2.0.CO;2

LaCasce, J. H., & Groeskamp, S. (2020). Baroclinic modes over rough bathymetry and the surface deformation radius. *Journal of Physical Oceanography*, *50*(10), 1–40. https://doi.org/10.1175/jpo-d-20-0055.1

Ladd, C., Mordy, C. W., Salo, S. A., & Stabeno, P. J. (2016). Winter water properties and the Chukchi Polynya. *Journal of Geophysical Research: Oceans*, *121*(8), 5516–5534. https://doi.org/10.1002/2016JC011918

Li, M., Pickart, R. S., Spall, M. A., Weingartner, T. J., Lin, P., Moore, G. W. K., & Qi, Y. (2019). Circulation of the Chukchi Sea shelfbreak and slope from moored timeseries. *Progress in Oceanography*, *172*, 14–33. https://doi.org/10.1016/j.pocean.2019.01.002

Lin, P., Pickart, R. S., McRaven, L. T., Arrigo, K. R., Bahr, F., Lowry, K. E., et al. (2019). Water mass evolution and circulation of the northeastern Chukchi Sea in summer: Implications for nutrient distributions. *Journal of Geophysical Research: Oceans*, *124*(7), 4416–4432. https://doi.org/10.1029/2019JC015185

Llinás, L., Pickart, R. S., Mathis, J. T., & Smith, S. L. (2009). Zooplankton inside an Arctic Ocean cold-core eddy: Probable origin and fate. *Deep Sea Research Part II: Topical Studies in Oceanography*, *56*(17), 1290–1304. https://doi.org/10.1016/j.dsr2.2008.10.020

Lowry, K. E., Pickart, R. S., Mills, M. M., Brown, Z. W., van Dijken, G. L., Bates, N. R., & Arrigo, K. R. (2015). The influence of winter water on phytoplankton blooms in the Chukchi Sea. *Deep Sea Research Part II: Topical Studies in Oceanography*, *118*, 53–72. https://doi.org/10.1016/j.dsr2.2015.06.006

Lowry, K. E., Pickart, R. S., Selz, V., Mills, M. M., Pacini, A., Lewis, K. M., et al. (2018). Under-ice phytoplankton blooms inhibited by spring convective mixing in refreezing leads. *Journal of Geophysical Research: Oceans*, *123*(1), 90–109. https://doi.org/10.1002/2016JC012575

Maas, L. R. M., & Van Haren, J. J. M. (1987). Observations on the vertical structure of tidal and inertial currents in the central North Sea. *Journal of Marine Research*, *45*(2), 293–318. https://doi.org/10.1357/002224087788401106

MacKinnon, J. A., & Gregg, M. C. (2005). Near-inertial waves on the New England shelf: The role of evolving stratification, turbulent dissipation, and bottom drag. *Journal of Physical Oceanography*, *35*(12), 2408–2424. https://doi.org/10.1175/JPO2822.1

Martini, K. I., Simmons, H. L., Stoudt, C. A., & Hutchings, J. K. (2014). Near-inertial internal waves and sea ice in the Beaufort Sea. *Journal of Physical Oceanography*, *44*(8), 2212–2234. https://doi.org/10.1175/JPO-D-13-0160.1

McPhee, M. G. (1978). A simulation of inertial oscillation in drifting pack ice. *Dynamics of Atmospheres and Oceans*, *2*(2), 107–122. https://doi.org/10.1016/0377-0265(78)90005-2

Mesinger, F., DiMego, G., Kalnay, E., Mitchell, K., Shafran, P. C., Ebisuzaki, W., et al. (2006). North American regional reanalysis. *Bulletin of the American Meteorological Society*, *87*(3), 343–360. https://doi.org/10.1175/BAMS-87-3-343

Morison, J. H., Long, C. E., & Levine, M. D. (1985). Internal wave dissipation under sea ice. *Journal of Geophysical Research*, *90*(C6), 11959–11966. https://doi.org/10.1029/JC090iC06p11959

Padman, L., & Erofeeva, S. (2004). A barotropic inverse tidal model for the Arctic Ocean. *Geophysical Research Letters*, *31*(2), L02303. https://doi.org/10.1029/2003GL019003

Padman, L., Erofeeva, S., & Howard, S. (2020). *AOTIM5: Arctic ocean inverse tide model, on 5 kilometer grid, developed in 2004*. Arctic Data Center. https://doi.org/10.18739/A2S17SS80

Park, J. H., & Watts, D. R. (2006). Internal tides in the southwestern Japan/East Sea. *Journal of Physical Oceanography*, *36*(1), 22–34. https://doi.org/10.1175/JPO2846.1

Pawlowicz, R., Beardsley, B., & Lentz, S. (2002). Classical tidal harmonic analysis including error estimates in MATLAB using T_TIDE. *Computers & Geosciences*, *28*(8), 929–937. https://doi.org/10.1016/S0098-3004(02)00013-4

Pickart, R. S., Moore, G. W. K., Mao, C., Bahr, F., Nobre, C., & Weingartner, T. J. (2016). Circulation of winter water on the Chukchi shelf in early Summer. *Deep Sea Research Part II: Topical Studies in Oceanography*, *130*, 56–75. https://doi.org/10.1016/j.dsr2.2016.05.001

Plueddemann, A. J., Krishfield, R., Takizawa, T., Hatakeyama, K., & Honjo, S. (1998). Upper ocean velocities in the Beaufort Gyre. *Geophysical Research Letters*, *25*(2), 183–186. https://doi.org/10.1029/97GL53638

Pnyushkov, A. V., & Polyakov, I. V. (2012). Observations of tidally induced currents over the continental slope of the Laptev Sea, Arctic Ocean. *Journal of Physical Oceanography*, *42*(1), 78–94. https://doi.org/10.1175/JPO-D-11-064.1

Pollard, R. T., & Millard, R. C. (1970). Comparison between observed and simulated wind-generated inertial oscillations. *Deep-Sea Research and Oceanographic Abstracts*, *17*(4), 813–821. https://doi.org/10.1016/0011-7471(70)90043-4

Poulain, P.-M., & Centurioni, L. (2015). Direct measurements of World Ocean tidal currents with surface drifters. *Journal of Geophysical Research: Oceans*, *120*(10), 6986–7003. https://doi.org/10.1002/2015JC010818

Rainville, L., & Woodgate, R. a. (2009). Observations of internal wave generation in the seasonally ice-free Arctic. *Geophysical Research Letters*, *36*(23), L23604. https://doi.org/10.1029/2009GL041291

Schulze, L. M., & Pickart, R. S. (2012). Seasonal variation of upwelling in the Alaskan Beaufort Sea: Impact of sea ice cover. *Journal of Geophysical Research*, *117*(C6), C06022. https://doi.org/10.1029/2012JC007985

Spall, M. A. (2007). Circulation and water mass transformation in a model of the Chukchi Sea. *Journal of Geophysical Research*, *112*(C5), C05025. https://doi.org/10.1029/2005JC003364

Stabeno, P., Kachel, N., Ladd, C., & Woodgate, R. (2018). Flow patterns in the eastern Chukchi Sea: 2010–2015. *Journal of Geophysical Research: Oceans*, *123*(2), 1177–1195. https://doi.org/10.1002/2017JC013135

Stoudt, C. A. (2015). Sea ice near-inertial response to atmospheric storms. (Order No. 1588390). Available from Dissertations & Theses @ University of Alaska Fairbanks. (1682267616) (p. 76). Retrieved from https://Search.Proquest.Com/Docview/1682267616?Accountid=14470

Visbeck, M., & Fischer, J. (1994). Sea surface conditions remotely sensed by upward-looking ADCPs. *Journal of Atmospheric and Oceanic Technology*, *12*(1), 141–149. https://doi.org/10.1175/1520-0426(1995)012<0141:SSCRSB>2.0.CO;2

Wang, J., Flierl, G. R., Lacasce, J. H., Mcclean, J. L., & Mahadevan, A. (2013). Reconstructing the ocean's interior from surface data. *Journal of Physical Oceanography*, *43*(8), 1611–1626. https://doi.org/10.1175/JPO-D-12-0204.1

Watanabe, E., Onodera, J., Itoh, M., & Mizobata, K. (2022). Transport processes of Seafloor Sediment from the Chukchi shelf to the Western Arctic Basin. *Journal of Geophysical Research: Oceans*, *127*(4), e2021JC017958. https://doi.org/10.1029/2021JC017958

Watanabe, E., Onodera, J., Itoh, M., Nishino, S., & Kikuchi, T. (2017). Winter transport of subsurface warm water toward the Arctic Chukchi Borderland. *Deep-Sea Research Part I Oceanographic Research Papers*, *128*, 115–130. https://doi.org/10.1016/j.dsr.2017.08.009

Weingartner, T. J., Aagaard, K., Woodgate, R., Danielson, S., Sasaki, Y., & Cavalieri, D. (2005). Circulation on the north central Chukchi Sea shelf. *Deep Sea Research Part II: Topical Studies in Oceanography*, *52*(24–26), 3150–3174. https://doi.org/10.1016/j.dsr2.2005.10.015

Weingartner, T. J., Cavalieri, D. J., Aagaard, K., & Sasaki, Y. (1998). Circulation, dense water formation, and outflow on the northeast Chukchi Shelf. *Journal of Geophysical Research*, *103*(C4), 7647–7661. https://doi.org/10.1029/98JC00374

Weingartner, T. J., Danielson, S. L., Potter, R. A., Trefry, J. H., Mahoney, A., Savoie, M., et al. (2017). Circulation and water properties in the landfast ice zone of the Alaskan Beaufort Sea. *Continental Shelf Research*, *148*, 185–198. https://doi.org/10.1016/j.csr.2017.09.001

Weingartner, T. J., Dobbins, E., Fang, Y.-C., Statscewich, H., & Stoudt, C. (2022). *Currents, Ice Velocity, Temperature, and Salinity from moorings around Hanna Shoal, Chukchi Sea, 2012–2014*. Arctic Data Center. https://doi.org/10.18739/A25M6280M

Weingartner, T. J., Fang, Y.-C., Winsor, P., Dobbins, E., Potter, R., Statscewich, H., et al. (2017). The summer hydrographic structure of the Hanna Shoal region on the northeastern Chukchi Sea shelf: 2011–2013. *Deep Sea Research Part II: Topical Studies in Oceanography*, *144*, 6–20. https://doi.org/10.1016/j.dsr2.2017.08.006

Werner, S. R., Beardsley, R. C., Lentz, S. J., Hebert, D. L., & Oakey, N. S. (2003). Observations and modelling of the tidal bottom boundary layer on the southern flank of Georges Bank. *Journal of Geophysical Research C: Oceans*, *108*(11), 8005. https://doi.org/10.1029/2001jc001271

Woodgate, R. A. (2018). Increases in the Pacific inflow to the Arctic from 1990 to 2015, and insights into seasonal trends and driving mechanisms from year-round Bering Strait mooring data. *Progress in Oceanography*, *160*(December), 124–154. https://doi.org/10.1016/j.pocean.2017.12.007

Woodgate, R. A., Weingartner, T. J., & Lindsay, R. (2012). Observed increases in Bering Strait oceanic fluxes from the Pacific to the Arctic from 2001 to 2011 and their impacts on the Arctic Ocean water column. *Geophysical Research Letters*, *39*(24), 2012GL054092. https://doi.org/10.1029/2012GL054092

Wunsch, C. (1975). Internal tides in the ocean. *Reviews of Geophysics*, *13*(1), 167–182. https://doi.org/10.1029/RG013i001p00167

Wunsch, C. (1997). The vertical partition of oceanic horizontal kinetic energy. *Journal of Physical Oceanography*, *27*(8), 1770–1794. https://doi.org/10.1175/1520-0485(1997)027<1770:TVPOOH>2.0.CO;2

Yang, J. (2006). The seasonal variability of the Arctic Ocean Ekman transport and its role in the mixed layer heat and Salt fluxes. *Journal of Climate*, *19*(20), 5366–5387. https://doi.org/10.1175/JCLI3892.1

Zhao, Z., Alford, M. H., MacKinnon, J. A., & Pinkel, R. (2010). Long-range propagation of the semidiurnal internal tide from the Hawaiian ridge. *Journal of Physical Oceanography*, *40*(4), 713–736. https://doi.org/10.1175/2009JPO4207.1